Journal of Non-Newtonian Fluid Mechanics 247 (2017) 90–106

Contents lists available at ScienceDirect

Journal of Non-Newtonian Fluid Mechanics

journal homepage: www.elsevier.com/locate/jnnfm

# A three-field local projection stabilized formulation for computations of Oldroyd-B viscoelastic fluid flows

Jagannath Venkatesan, Sashikumaar Ganesan*

*Department of Computational and Data Sciences, Indian Institute of Science, Bangalore 560012, India*

ARTICLE INFO

*Article history:*
Received 16 January 2017
Revised 3 June 2017
Accepted 25 June 2017
Available online 27 June 2017

*Keywords:*
Local Projection Stabilization
Finite elements
Viscoelastic fluids
Oldroyd-B model

ABSTRACT

A new three-field formulation based on the Local Projection Stabilization (LPS) is developed for computations of the coupled Navier–Stokes and Oldroyd-B viscoelastic constitutive equations at high Weissenberg numbers. One-level LPS is based on an enriched approximation space and a discontinuous projection space, where both spaces are defined on a same mesh. It allows us to use equal order interpolation spaces for the velocity and the viscoelastic stress, whereas inf-sup stable finite elements are used for the velocity and the pressure. Further, the coupled system of equations are solved in a monolithic approach. Since the stabilization terms in LPS are assembled only once, the proposed scheme is computationally efficient in comparison with residual based stabilized numerical schemes. Numerical studies using method of manufactured solutions show an optimal order of convergence in the respective norms. Further, the proposed scheme is validated using two benchmark problems: flow past a cylinder in a rectangular channel and lid-driven cavity flow. Moreover, the numerical results are compared with the results in the literature and the effects of elasticity and inertia are studied.



## 1. Introduction

Viscoelastic flows can be found in a wide range of industrial and commercial applications such as enhanced oil recovery, pesticide deposition, medicinal/pharmaceutical sprays, drug delivery, injection molding, polymer melts, inkjet printing, additive manufacturing, cosmetics industry and food processing. Flows of viscoelastic fluids are very complex in nature and often result in complex secondary flows and transient flow patterns even in very simple geometries. A quantitative understanding of the flow dynamics of viscoelastic fluids is essential to predict optimal processing conditions to improve the quality of the final products in various industrial and commercial applications.

Mathematical models of viscoelastic fluid flows can be classified into two categories: kinetic theory models and continuum mechanics models. The kinetic theory approach attempts to model the polymer dynamics by using a coarse-grained description of polymer chains by representing them as chains of springs or rods which eventually lead to Fokker–Planck equation. Continuum approach attempts to provide constitutive differential equations, where the micro properties are obtained empirically. Oldroyd-B [1], Giesekus [2], finitely extensible non-linear elastic (FENE-P [3], FENE-CR [4]), Phan-Thien-Tanner (PTT) [5] and eXtended Pom-Pom (XPP) [6] are the commonly used continuum models in the literature. Since the focus of this paper is to develop an efficient numerical scheme for viscoelastic fluid flows, the continuum mechanics approach and in particular the Oldroyd-B model is considered. Oldroyd-B model is the simplest model and utilized very often for various viscoelastic benchmark problems. Its generality is well-accepted by the CFD community to test different numerical methods and formulations even though this model has an infinite extensional viscosity that leads to a non-physical stress growth in the direction of the extensional flow. Due to the inherent complexity of viscoelastic fluids and the resulting analytic intractability of the mathematical models in this area, computational approaches are playing an ever increasing role. Numerical simulations are not only cost-effective, but also allow the study of problems where experiments are unfeasible and theoretical predictions are very difficult or nearly impossible to obtain.

Numerical simulations of isothermal, incompressible viscoelastic flows involve simultaneous solution of the Navier–Stokes equations and a viscoelastic constitutive equation. Although a considerable progress has been made in the literature, many challenges still remain in computations of viscoelastic fluid flows. The constitutive equation is highly advection dominated which may induce both global and local oscillations in the numerical solution. Further, the choice of the approximation spaces for the velocity, the pressure and the viscoelastic stress is restricted by the compati-

* Corresponding author.
*E-mail addresses:* jagan@cmg.cds.iisc.ac.in (J. Venkatesan), sashi@cds.iisc.ac.in (S. Ganesan).

http://dx.doi.org/10.1016/j.jnnfm.2017.06.007
0377-0257/

bility conditions. In addition, all numerical schemes that simulate viscoelastic flows encounter a major challenge: the so-called high Weissenberg number problem (HWNP), i.e. a difficulty in obtaining mesh-converged numerical solutions even for simple benchmark problems at high Weissenberg numbers. Weissenberg number (Wi) is a non-dimensional measure of the elasticity of the fluid. At high Weissenberg numbers, the stress experiences a combination of deformation and convection, which gives rise to steep exponential profiles. Thus, the spatial profiles of the viscoelastic stress are poorly approximated by the numerical schemes, which use polynomial basis functions. The failure to properly balance the deformation with the convection yields a numerical instability. It has been shown by Hulsen [7] that the stress field needs to be positive-definite throughout the computations to avoid numerical instabilities. It can be achieved by rewriting the stress equation in terms of conformation stress tensor, which is symmetric positive-definite [7]. Fattal and Kupferman [8] proposed a log-conformation representation (LCR) method. In LCR method, the constitutive relations have been reformulated as equations for the logarithm of the conformation tensor which allows to compute stress at high Weissenberg numbers. Recently, Knechtges et al. [9] have proposed a fully implicit way of handling the log-conformation transformation which avoids the eigen-decomposition of the velocity gradient. Alternatively, Balci et al. [10] have proposed a square-root conformation representation to handle HWNP. In addition, a kernel conformation tensor transformation for computations of viscoelastic fluid flows has been proposed by Afonso et al. [11].

In order to handle dominated convection and/or to use equal order interpolation spaces for the velocity and the viscoelastic stress, various stabilization approaches have been proposed in the literature and we briefly review it here. The most widespread method to suppress the spurious oscillations that occur due to the advection dominated constitutive equation is the Streamline Upwind Petrov Galerkin (SUPG) method of Brooks and Hughes [12], and it has first been applied to viscoelastic flows by Marchal and Crochet [13]. Subsequently, several stabilization techniques such as Elastic Viscous Stress Splitting (EVSS) [14], Discrete Elastic Viscous Stress Splitting (DEVSS) [15,16], Explicitly Elliptic Momentum Equation (EEME) [17], Discrete adaptive viscoelastic stress splitting (DAVSS) [18] and the Discontinuous Galerkin (DG) method [19] have been proposed in the literature.

In addition, Fan et al. [20] introduced an incomplete Galerkin Least Squares (GLS) method and Coronado et al. [21] proposed a complete four–field GLS method for viscoelastic flows. Li et al. [22] proposed I-PS-DEVSS-CNBS scheme, which is based on the finite incremental calculus (FIC), pressure stabilization process, DEVSS method, the use of the Crank–Nicolson-based-splitting (CNBS) scheme and the use of the non-consistent SUPG method to stabilize the viscoelastic constitutive equation. Further, a fully explicit characteristic based split scheme for viscoelastic fluids has been proposed by Nithiarasu [23]. Also, Chen et. al. [24] introduced a least square technique for viscoelastic flows and Lee [25] proposed a nonlinear weighted least-squares finite element method for Oldroyd-B flows. Kwack and Masud [26] used a residual based Variational Multi-Scale (VMS) stabilized method for the momentum equation and SUPG method for the constitutive equation. Recently, Castillo and Codina [27] proposed two stabilized formulations based on the VMS framework, namely algebraic sub-grid scale method and orthogonal sub-grid scale method to handle the convective nature of the viscoelastic constitutive equation.

In the present work, we propose an alternative approach based on the Local Projection Stabilization (LPS) to handle the convective nature of the viscoelastic constitutive equation and to use equal order interpolation spaces for the velocity and the viscoelastic stress. Originally proposed for the Stokes problem by Becker and Braack [28], LPS has been extended successfully for transport [29] and Oseen [30] problems. The stabilization term of the local projection method is based on a projection $\pi_h$: $Y_h \rightarrow D_h$ of the finite element space $Y_h$, which approximates the solution, into a discontinuous space $D_h$. In LPS, the standard Galerkin discretization is stabilized by adding a term that gives $L^2$ control over the fluctuation $id - \pi_h$ of the gradient of the solution, where $id$ is the identity mapping. In all these papers [28–30], a two-level approach has been used where the projection space $D_h$ is defined on a mesh that is coarser than the mesh used for the approximation space $Y_h$. This approach leads to computations on two different meshes. To use a single mesh, an one-level approach based on enrichment of the approximation space has been proposed in [31–33]. Refer the review paper by Braack and Lube [34] for more details on LPS. In this work, we use the one-level LPS scheme for numerical simulation of steady-state and transient Oldroyd-B viscoelastic fluid flows at high Weissenberg numbers.

To validate the proposed numerical scheme for Oldroyd-B viscoelastic flows, we present numerical results for two benchmark problems: flow past a cylinder in a rectangular channel [9,18,20,21,26,35–37] and lid-driven cavity flow [8,37–42]. Further, the effects of elasticity and inertia on the flow dynamics of viscoelastic fluids in the considered benchmark problems are analyzed. In addition, a convergence study based on the method of manufactured solutions is performed to numerically check the rate of convergence of the proposed stabilized formulation for Oldroyd-B viscoelastic fluid flows.

The paper is organized as follows: description of the governing equations of viscoelastic fluid flow and its dimensionless form are presented in Section 2. In Section 3, the weak form of the model equations and the Galerkin finite element discretization for the considered problem are outlined. Further, a stabilization technique based on one-level LPS is designed for computations of Oldroyd-B viscoelastic flows at high Weissenberg numbers. In addition, the temporal discretization and linearization strategy used in the numerical scheme are outlined. Numerical results are presented in Section 4 and finally conclusions are summarized in Section 5.

## 2. Mathematical model

### 2.1. Governing equations of viscoelastic fluid flow

The flow of an incompressible, isothermal viscoelastic fluid in a bounded domain $\Omega \subset \mathbb{R}^2$ and in the time interval $t \in (0, \mathrm{I}]$ is described by the Navier–Stokes equations:

$$\begin{aligned} \rho\left(\frac{\partial \mathbf{u}}{\partial t} + \mathbf{u}\cdot\nabla\mathbf{u}\right) - \nabla\cdot\mathbb{T}(\mathbf{u}, p, \boldsymbol{\sigma}) = 0 \quad &\text{in} \quad \Omega\times(0,\mathrm{I}], \\ \nabla\cdot\mathbf{u} = 0 \quad &\text{in} \quad \Omega\times(0,\mathrm{I}], \end{aligned} \tag{1}$$

where $\rho$, $t$, $\mathbf{u}$, $p$, $\boldsymbol{\sigma}$ and I denote the fluid density, time, velocity, pressure, viscoelastic stress and given end time, respectively. Here, the stress tensor $\mathbb{T}(\mathbf{u}, p, \boldsymbol{\sigma})$ that incorporates the effect of viscoelastic stress is given by

$$\mathbb{T}(\mathbf{u}, p, \boldsymbol{\sigma}) = -p\mathbb{I} + 2\mu_s\mathbb{D}(\mathbf{u}) + \boldsymbol{\sigma}, \tag{2}$$

where $\mathbb{I}$ and $\mu_s$ denote the identity tensor and the viscosity of Newtonian solvent, respectively. Note that the first two terms in equation (2) are the stress contributions from the Newtonian solvent, whereas the last term is the stress contribution from the polymeric solute. Further, the velocity deformation tensor $\mathbb{D}(\mathbf{u})$ is given by

$$\mathbb{D}(\mathbf{u}) = \frac{1}{2}\left(\nabla\mathbf{u} + \nabla\mathbf{u}^{\mathrm{T}}\right),$$

where the superscript T denotes transpose. The transient evolution of the viscoelastic stress in the fluid can be described by a consti-

tutive equation of differential type, see for example [1–6]. In this work, we consider the Oldroyd-B [1] constitutive model given by

$$\lambda \overset{\nabla}{\boldsymbol{\sigma}} + \boldsymbol{\sigma} - 2\mu_p \mathbb{D}(\mathbf{u}) = 0 \quad \text{in} \quad \Omega \times (0, \mathrm{I}], \tag{3}$$

where $\lambda$ and $\mu_p$ denote the relaxation time and polymeric viscosity, respectively. Further, the upper-convected time derivative of the viscoelastic stress tensor is defined as

$$\overset{\nabla}{\boldsymbol{\sigma}} = \frac{\partial \boldsymbol{\sigma}}{\partial t} + \mathbf{u} \cdot \nabla \boldsymbol{\sigma} - (\nabla \mathbf{u})^{\mathrm{T}} \cdot \boldsymbol{\sigma} - \boldsymbol{\sigma} \cdot (\nabla \mathbf{u}).$$

Next, the dimensionless conformation stress tensor ($\boldsymbol{\tau}$), which has the positive definite property [7], is given by the following relation

$$\boldsymbol{\sigma} = \frac{\mu_p}{\lambda}(\boldsymbol{\tau} - \mathbb{I}).$$

Rewriting the Oldroyd-B constitutive equation (3) in terms of the conformation stress tensor using the above relation, we get

$$\frac{\partial \boldsymbol{\tau}}{\partial t} + \mathbf{u} \cdot \nabla \boldsymbol{\tau} - (\nabla \mathbf{u})^{\mathrm{T}} \cdot \boldsymbol{\tau} - \boldsymbol{\tau} \cdot (\nabla \mathbf{u}) + \frac{1}{\lambda}(\boldsymbol{\tau} - \mathbb{I}) = 0. \tag{4}$$

The coupled Navier–Stokes (1) and Oldroyd-B constitutive equations (4) are closed with the initial and boundary conditions. At time $t = 0$, we specify the conformation stress tensor $\boldsymbol{\tau}_0$ and the divergence-free velocity field $\mathbf{u}_0$ over the entire computational domain, i.e.,

$$\mathbf{u}(\cdot, 0) = \mathbf{u}_0, \quad \boldsymbol{\tau}(\cdot, 0) = \boldsymbol{\tau}_0 \quad \text{in} \quad \Omega. \tag{5}$$

The boundary conditions for different examples investigated in this work are described in Section 4. Nevertheless, for deriving the weak formulation, we impose a non-homogeneous Dirichlet boundary condition for the velocity over the entire boundary $\partial\Omega$, i.e.,

$$\mathbf{u} = \mathbf{u}_d \quad \text{on} \quad \partial\Omega. \tag{6}$$

### 2.2. Dimensionless form of model equations

In this section, we derive the dimensionless form of the coupled Navier–Stokes (1) and the Oldroyd-B constitutive equations (4). We introduce the scaling factors L and U as the characteristic length and velocity, respectively. Further, we define the dimensionless variables

$$\tilde{x} = \frac{x}{\mathrm{L}}, \quad \tilde{\mathbf{u}} = \frac{\mathbf{u}}{\mathrm{U}}, \quad \tilde{t} = \frac{t\mathrm{U}}{\mathrm{L}}, \quad \tilde{\mathrm{I}} = \frac{\mathrm{IU}}{\mathrm{L}}, \quad \tilde{p} = \frac{p}{\rho \mathrm{U}^2}, \quad \tilde{\boldsymbol{\tau}} = \boldsymbol{\tau}$$

and the dimensionless numbers (Reynolds, Weissenberg and amount of solvent contribution, respectively)

$$\mathrm{Re} = \frac{\rho \mathrm{UL}}{\mu_0}, \quad \mathrm{Wi} = \frac{\lambda \mathrm{U}}{\mathrm{L}}, \quad \beta = \frac{\mu_s}{\mu_0}.$$

Here, $\mu_0 = \mu_s + \mu_p$ denotes the total viscosity. Writing the coupled system in a dimensionless form and omitting the tilde afterwards, we end up with the following dimensionless Navier–Stokes and Oldroyd-B constitutive equations:

$$\begin{aligned} \frac{\partial \mathbf{u}}{\partial t} + \mathbf{u} \cdot \nabla \mathbf{u} - \frac{2\beta}{\mathrm{Re}} \nabla \cdot \mathbb{D}(\mathbf{u}) + \nabla p - \frac{(1-\beta)}{\mathrm{ReWi}} \nabla \cdot \boldsymbol{\tau} = 0, \\ \nabla \cdot \mathbf{u} = 0, \\ \frac{\partial \boldsymbol{\tau}}{\partial t} + \mathbf{u} \cdot \nabla \boldsymbol{\tau} - (\nabla \mathbf{u})^{\mathrm{T}} \cdot \boldsymbol{\tau} - \boldsymbol{\tau} \cdot (\nabla \mathbf{u}) + \frac{1}{\mathrm{Wi}}(\boldsymbol{\tau} - \mathbb{I}) = 0. \end{aligned} \tag{7}$$

Here, the unknown components of the velocity and the conformation stress tensor are denoted by

$$\mathbf{u} = (u_x, \ u_y)^{\mathrm{T}} \ \text{and} \ \boldsymbol{\tau} = \begin{bmatrix} \tau_{xx} & \tau_{xy} \\ \tau_{yx} & \tau_{yy} \end{bmatrix} \text{with } \tau_{yx} = \tau_{xy}.$$

## 3. Numerical scheme

### 3.1. Weak formulation

Let $L^2(\Omega)$ and $H^1(\Omega)$ be the standard Sobolev spaces and $(\cdot, \cdot)$ be the inner product in $L^2(\Omega)$ and its vector/tensor-valued versions, respectively. Further, we define the ansatz spaces for the velocity, pressure, viscoelastic conformation stress and the test space for the velocity as

$$\begin{aligned} V &:= \left\{ \mathbf{v} \in H^1(\Omega)^2 \right\}, \\ Q &:= \left\{ q \in L^2(\Omega) : \int_\Omega q dx = 0 \right\}, \\ S &:= \left\{ \psi = \left[\psi_{ij}\right], 1 \le i, j \le 2, \ \ \psi_{ij} \in H^1(\Omega), \ \ \psi_{ij} = \psi_{ji} \right\}, \\ V_0 &:= \left\{ \mathbf{v} \in H^1(\Omega)^2 : \mathbf{v} = 0 \ \text{ on } \ \partial\Omega \right\}. \end{aligned}$$

We now multiply the momentum balance, the mass balance and the conformation stress tensor equations (7), by test functions $\mathbf{v} \in V_0$, $q \in Q$ and $\boldsymbol{\psi} \in S$, respectively and integrate over $\Omega$. After applying integration by parts to the stress tensor term in the momentum balance equation (first equation in (7)), we get the following weak form of the model problem:

For given $\mathbf{u}_0$, $\mathbf{u}_d$ and $\boldsymbol{\tau}_0$, find $(\mathbf{u}, p, \boldsymbol{\tau}) \in V \times Q \times S$ such that

$$\begin{aligned} \left( \frac{\partial \mathbf{u}}{\partial t}, \mathbf{v} \right) + a(\hat{\mathbf{u}}; \mathbf{u}, \mathbf{v}) - b(p, \mathbf{v}) + c(\boldsymbol{\tau}, \mathbf{v}) = 0, \\ b(q, \mathbf{u}) = 0, \\ \left( \frac{\partial \boldsymbol{\tau}}{\partial t}, \psi \right) + d(\hat{\mathbf{u}}, \boldsymbol{\tau}, \boldsymbol{\psi}) + e(\boldsymbol{\tau}, \boldsymbol{\psi}) = f(\boldsymbol{\psi}), \end{aligned} \tag{8}$$

for all $(\mathbf{v}, q, \boldsymbol{\psi}) \in V_0 \times Q \times S$ , where

$$\begin{aligned} a(\hat{\mathbf{u}}; \mathbf{u}, \mathbf{v}) &= \frac{2\beta}{\mathrm{Re}} \int_\Omega \mathbb{D}(\mathbf{u}) : \mathbb{D}(\mathbf{v}) \ dx + \int_\Omega (\hat{\mathbf{u}} \cdot \nabla)\mathbf{u} \cdot \mathbf{v} \ dx \\ b(q, \mathbf{v}) &= \int_\Omega q \nabla \cdot \mathbf{v} \ dx \\ c(\boldsymbol{\tau}, \mathbf{v}) &= \frac{(1-\beta)}{\mathrm{ReWi}} \int_\Omega \boldsymbol{\tau} : \mathbb{D}(\mathbf{v}) \, dx \\ d(\hat{\mathbf{u}}, \boldsymbol{\tau}, \boldsymbol{\psi}) &= \int_\Omega (\hat{\mathbf{u}} \cdot \nabla \boldsymbol{\tau}) : \boldsymbol{\psi} \, dx - \int_\Omega (\nabla \hat{\mathbf{u}}^{\mathrm{T}} \cdot \boldsymbol{\tau} + \boldsymbol{\tau} \cdot \nabla \hat{\mathbf{u}}) : \boldsymbol{\psi} \, dx \\ e(\boldsymbol{\tau}, \boldsymbol{\psi}) &= \frac{1}{\mathrm{Wi}} \int_\Omega \boldsymbol{\tau} : \boldsymbol{\psi} \, dx \\ f(\boldsymbol{\psi}) &= \frac{1}{\mathrm{Wi}} \int_\Omega \mathbb{I} : \boldsymbol{\psi} \ dx. \end{aligned}$$

Here, the notation $\hat{\mathbf{u}}$ is used to indicate the nonlinear term. Since the coupled system is solved in a monolithic approach, we rewrite the above weak formulation in a compact form:

For given $\mathbf{u}_0$, $\mathbf{u}_d$ and $\boldsymbol{\tau}_0$, find $(\mathbf{u}, p, \boldsymbol{\tau}) \in V \times Q \times S$ such that

$$\left( \frac{\partial \mathbf{u}}{\partial t}, \mathbf{v} \right) + A(\hat{\mathbf{u}}; (\mathbf{u}, p, \boldsymbol{\tau}), (\mathbf{v}, q, \boldsymbol{\psi})) + \left( \frac{\partial \boldsymbol{\tau}}{\partial t}, \boldsymbol{\psi} \right) = f(\boldsymbol{\psi}) \tag{9}$$

for all $(\mathbf{v}, q, \boldsymbol{\psi}) \in V_0 \times Q \times S$ , where

$$\begin{aligned} A(\hat{\mathbf{u}}; (\mathbf{u}, p, \boldsymbol{\tau}), (\mathbf{v}, q, \boldsymbol{\psi})) &= a(\hat{\mathbf{u}}; \mathbf{u}, \mathbf{v}) - b(p, \mathbf{v}) + c(\boldsymbol{\tau}, \mathbf{v}) \\ &+ b(q, \mathbf{u}) + d(\hat{\mathbf{u}}, \boldsymbol{\tau}, \boldsymbol{\psi}) + e(\boldsymbol{\tau}, \boldsymbol{\psi}). \end{aligned}$$

### 3.2. Spatial discretization

#### 3.2.1. Galerkin finite element

For the finite element discretization of (9), let $\{\mathcal{T}_h\}$ denote a family of shape-regular decomposition of $\Omega$ into triangles or quadrilaterals. The diameter of a cell $K \in \mathcal{T}_h$ is denoted by $h_K$. The mesh parameter $h$ is the maximum diameter of among all cells in $\mathcal{T}_h$. Let $V_h \subset V$, $Q_h \subset Q$ and $S_h \subset S$ be the conforming finite element

spaces on $\mathcal{T}_h$. The standard Galerkin approximation of the variational problem (9) reads:

For given $\mathbf{u}_0$, $\mathbf{u}_d$ and $\boldsymbol{\tau}_0$, find $(\mathbf{u}_h, p_h, \boldsymbol{\tau}_h) \in V_h \times Q_h \times S_h$ such that

$$\left(\frac{\partial \mathbf{u}_h}{\partial t}, \mathbf{v}_h\right) + A(\hat{\mathbf{u}}_h; (\mathbf{u}_h, p_h, \boldsymbol{\tau}_h), (\mathbf{v}_h, q_h, \boldsymbol{\psi}_h)) + \left(\frac{\partial \boldsymbol{\tau}_h}{\partial t}, \boldsymbol{\psi}_h\right) = f(\boldsymbol{\psi}_h) \tag{10}$$

for all $(\mathbf{v}_h, q_h, \boldsymbol{\psi}_h) \in V_{h,0} \times Q_h \times S_h$. In order to obtain a stable numerical scheme, the velocity space $V_h$ and the pressure space $Q_h$ need to be chosen in such a way that the discrete inf-sup condition,

$$\inf_{q_h \in Q_h} \sup_{\mathbf{v}_h \in V_h} \frac{\left(q_h, \nabla \cdot \mathbf{v}_h\right)}{\|q_h\|_{Q_h} \|\mathbf{v}_h\|_{V_h}} \geq \beta_1 > 0, \tag{11}$$

holds true. Simultaneously, the conformation stress space $S_h$ and the velocity space $V_h$ should also satisfy the discrete inf-sup condition

$$\inf_{\mathbf{v}_h \in V_h} \sup_{\boldsymbol{\tau}_h \in S_h} \frac{\left(\boldsymbol{\tau}_h, \mathbb{D}(\mathbf{v}_h)\right)}{\|\boldsymbol{\tau}_h\|_{S_h} \|\mathbf{v}_h\|_{V_h}} \geq \beta_2 > 0. \tag{12}$$

These two requirements drastically reduce the choice of finite element spaces that allow stable discretization. For Stokes problem, Marchal and Crochet [13] have proposed a family of bi-quadratic velocity element $Q_2$, bilinear pressure element $Q_1$ and a family of $(2 \times 2)-$, $(3 \times 3)-$, $(4 \times 4)$-bilinear stress elements, which are defined on 4, 9 and 16 squares that are obtained by equally subdividing the reference quadrilateral. Nevertheless, the use of $(2 \times 2)-$, $(3 \times 3)-$bilinear stress elements do not lead to a stable scheme [43]. Further, $Q_3$ element has been suggested in [43] for stress approximation. Alternatively, discontinuous interpolations for the stresses has been proposed by Fortin and Fortin [19]. We refer to Baaijens [44,45] for a review of mixed finite element formulation for viscoelastic flows.

### 3.2.2. Local projection stabilized formulation

The standard Galerkin approach for solving the coupled Navier–Stokes and Oldroyd-B constitutive problem (10) may suffer in general from two shortcomings. First, the Oldroyd-B constitutive equation is highly advection dominated at high Weissenberg numbers. Second, the finite element spaces should satisfy the discrete inf-sup conditions (11) and (12) to have control over $p_h$ and $\mathbb{D}(\mathbf{u}_h)$, respectively. One way to overcome these difficulties is to use stabilized formulations. Even though numerical schemes that satisfy both inf-sup conditions are desired, it is seldom used for viscoelastic flow computations. Since a stabilized formulation is always needed to handle HWNP, equal order interpolation spaces for the velocity and the viscoelastic stress is preferred to avoid higher computational cost associated with the finite element pairs that satisfy the inf-sup condition. Stability and convergence analysis for different stabilization schemes with arbitrary order of interpolation spaces have been performed in the literature, see for example [46–50].

Residual based stabilization methods can circumvent the above two shortcomings and have been studied thoroughly in the literature [13–16,26] for viscoelastic flows. A drawback of the residual based methods is that they introduce a large number of additional coupling terms between the variables, which do not have any physical interpretation. An alternative to residual based methods is the symmetric stabilization method such as Local Projection Stabilization (LPS) [28–34], which have been investigated for convection-diffusion-reaction equations and Newtonian fluid flows in the literature.

In this work, we add symmetric stabilization terms to the standard Galerkin formulation (10) using one-level LPS method [31,32]. Local projection stabilization circumvents the spurious oscillations that occur due to advection dominated constitutive equation. Apart from this, LPS also allows to circumvent the inf-sup conditions and to use equal order interpolations to discretize the unknown variables, refer [32]. Nevertheless, we use inf-sup stable finite elements for the velocity and pressure spaces, and equal order interpolation spaces for the velocity and conformation stress.

Let $Y_h$ denote the approximation space and $D_h$ be the discontinuous projection space defined on $\mathcal{T}_h$. Let $D_h(K) := \{d_h|_K : d_h \in D_h\}$ and $\pi_K : Y_h(K) \to D_h(K)$ the local $L^2$-projection into $D_h(K)$. Further, we define the global projection $\pi_h : Y_h \to D_h$ by $(\pi_h y)|_K := \pi_K(y|_K)$. The fluctuation operator $\kappa_h : Y_h \to Y_h$ is given by $\kappa_h := id - \pi_h$, where $id$ is the identity mapping. We apply these operators to vector/tensor valued functions in a component-wise manner. Adding symmetric stabilization terms to the discrete problem (10), leads to the following stabilized discrete form:

For given $\mathbf{u}_0$, $\mathbf{u}_d$ and $\boldsymbol{\tau}_0$, find $(\mathbf{u}_h, p_h, \boldsymbol{\tau}_h) \in V_h \times Q_h \times S_h$ such that

$$\left(\frac{\partial \mathbf{u}_h}{\partial t}, \mathbf{v}_h\right) + \left(\frac{\partial \boldsymbol{\tau}_h}{\partial t}, \boldsymbol{\psi}_h\right) + S_1(\mathbf{u}_h, \mathbf{v}_h) + S_2(\boldsymbol{\tau}_h, \boldsymbol{\psi}_h) + A(\hat{\mathbf{u}}_h; (\mathbf{u}_h, p_h, \boldsymbol{\tau}_h), (\mathbf{v}_h, q_h, \boldsymbol{\psi}_h)) = f(\boldsymbol{\psi}_h) \tag{13}$$

for all $(\mathbf{v}_h, q_h, \boldsymbol{\psi}_h) \in V_{h,0} \times Q_h \times S_h$, where

$$S_1(\mathbf{u}_h, \mathbf{v}_h) = \sum_{K \in \mathcal{T}_h} \alpha_1 \langle \kappa_h \mathbb{D}(\mathbf{u}_h), \kappa_h \mathbb{D}(\mathbf{v}_h) \rangle_K$$

$$S_2(\boldsymbol{\tau}_h, \boldsymbol{\psi}_h) = \sum_{K \in \mathcal{T}_h} \alpha_2 \left\langle \kappa_h \nabla \cdot \boldsymbol{\tau}_h, \kappa_h \nabla \cdot \boldsymbol{\psi}_h \right\rangle_K + \sum_{K \in \mathcal{T}_h} \alpha_3 \left\langle \kappa_h \nabla \boldsymbol{\tau}_h, \kappa_h \nabla \boldsymbol{\psi}_h \right\rangle_K.$$

Here $\alpha_1 = (1-\beta)c_1 h_K$, $\alpha_2 = c_2 h_K$, $\alpha_3 = c_3 h_K$, where $c_1$, $c_2$ and $c_3$ are user-chosen constants. In computations, we use inf-sup stable finite element pairs for the velocity and pressure. The term $S_1(\mathbf{u}_h, \mathbf{v}_h)$ provides control when the elastic contribution is high, i.e., when $\beta$ is small. The first term in $S_2(\boldsymbol{\tau}_h, \boldsymbol{\psi}_h)$ provides control on the divergence of the conformation stress and it allows to use equal order interpolation spaces for the velocity and the conformation stress. The second term in $S_2(\boldsymbol{\tau}_h, \boldsymbol{\psi}_h)$ ensures the stability of the constitutive equation in advection dominated case.

We use mapped finite element spaces in our numerical computations where the enriched approximation spaces on the reference cell $\hat{K}$ are given by

$$P_r^{bubble}(\hat{K}) := P_r(\hat{K}) \oplus \left(\hat{b}_\triangle \cdot P_{r-1}(\hat{K})\right)$$

$$Q_r^{bubble}(\hat{K}) := Q_r(\hat{K}) \oplus \operatorname{span}\left\{\hat{b}_\square \cdot \hat{x}_i^{r-1}, \quad i = 1, 2\right\},$$

where $r \geq 2$. Here, $\hat{b}_\triangle$ and $\hat{b}_\square$ are the cubic bubble and the bi-quadratic bubble functions on the reference triangle and quadrilateral, respectively. On triangular cells, we use $(Y_h, D_h) = \left(P_r^{bubble}, P_{r-1}^{disc}\right)$, see Fig. 1, whereas on quadrilateral cells, we use $(Y_h, D_h) = \left(Q_r^{bubble}, P_{r-1}^{disc}\right)$, see Fig. 2.

### 3.3. Temporal discretization and linearization

Let $0 = t^0 < t^1 < \cdots < t^N = \mathrm{I}$ be a decomposition of the given time interval [0, I] and $\delta t = t^{n+1} - t^n$, $n = 0, \ldots, N-1$, be the uniform time step. Further, let $\mathbf{u}_h^n(x)$, $p_h^n(x)$ and $\boldsymbol{\tau}_h^n(x)$ be the approximations of the solutions $\mathbf{u}$, $p$ and $\boldsymbol{\tau}$ respectively at $t = t^n$ and $x \in \mathcal{T}_h$. Applying the first order backward Euler time discretization to the coupled system (13), results in a sequence of stationary

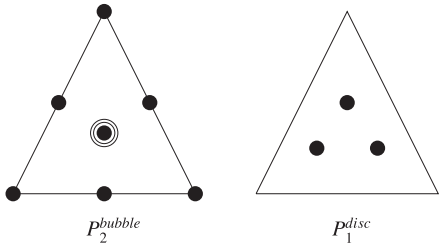


**Fig. 1.** Finite element pair $(Y_h, D_h) = \left(P_2^{bubble}, P_1^{disc}\right)$ used on triangular cells.

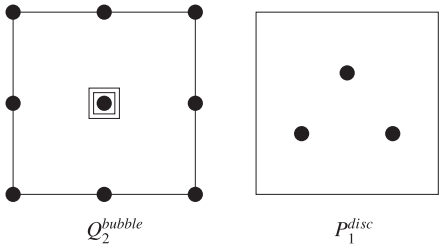


**Fig. 2.** Finite element pair $(Y_h, D_h) = \left(Q_2^{bubble}, P_1^{disc}\right)$ used on quadrilateral cells.

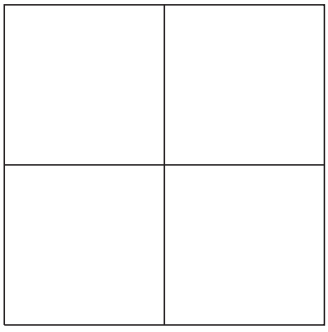

**Fig. 3.** Coarsest quadrilateral mesh (level 1) used in convergence test.

equations:

$$\left(\frac{\mathbf{u}_h^{n+1}-\mathbf{u}_h^n}{\delta t},\mathbf{v}_h\right)+a\left(\mathbf{u}_h^{n+1},\mathbf{u}_h^{n+1},\mathbf{v}_h\right)-b\left(p_h^{n+1},\mathbf{v}_h\right)+c\left(\boldsymbol{\tau}_h^{n+1},\mathbf{v}_h\right)+S_1\left(\mathbf{u}_h^{n+1},\mathbf{v}_h\right)=0,$$
$$b\left(q_h,\mathbf{u}_h^{n+1}\right)=0,$$
$$\left(\frac{\boldsymbol{\tau}_h^{n+1}-\boldsymbol{\tau}_h^n}{\delta t},\boldsymbol{\psi}_h\right)+d\left(\mathbf{u}_h^{n+1},\boldsymbol{\tau}_h^{n+1},\boldsymbol{\psi}_h\right)+e\left(\boldsymbol{\tau}_h^{n+1},\boldsymbol{\psi}_h\right)+S_2\left(\boldsymbol{\tau}_h^{n+1},\boldsymbol{\psi}_h\right)=f\left(\boldsymbol{\psi}_h\right). \quad (14)$$

Here, $a\left(\mathbf{u}_h^{n+1},\mathbf{u}_h^{n+1},\mathbf{v}_h\right)$ contains the non-linear convective velocity term in the Navier–Stokes equation, while $d\left(\mathbf{u}_h^{n+1},\boldsymbol{\tau}_h^{n+1},\boldsymbol{\psi}_h\right)$ contains the non-linear convection of stresses and rotational terms in the Oldroyd-B constitutive equation. We use an iteration of fixed point type to linearize the coupled system (14).

Let $\mathbf{u}_{h,0}^{n+1}=\mathbf{u}_h^n$, $\boldsymbol{\tau}_{h,0}^{n+1}=\boldsymbol{\tau}_h^n$ and $m=1,\ldots,\mathrm{M}$, where M is the maximum allowed number of non-linear iterations. We adopt the following linearization strategy in our computations:

$$a\left(\mathbf{u}_h^{n+1},\mathbf{u}_h^{n+1},\mathbf{v}_h\right)\approx a\left(\mathbf{u}_{h,m-1}^{n+1},\mathbf{u}_{h,m}^{n+1},\mathbf{v}_h\right)$$
$$d\left(\mathbf{u}_h^{n+1},\boldsymbol{\tau}_h^{n+1},\boldsymbol{\psi}_h\right)\approx d\left(\mathbf{u}_{h,m-1}^{n+1},\boldsymbol{\tau}_{h,m}^{n+1},\boldsymbol{\psi}_h\right)+d\left(\mathbf{u}_{h,m}^{n+1},\boldsymbol{\tau}_{h,m-1}^{n+1},\boldsymbol{\psi}_h\right)-d\left(\mathbf{u}_{h,m-1}^{n+1},\boldsymbol{\tau}_{h,m-1}^{n+1},\boldsymbol{\psi}_h\right).$$

After linearization, the coupled system (14) leads to the following system of linear equations:

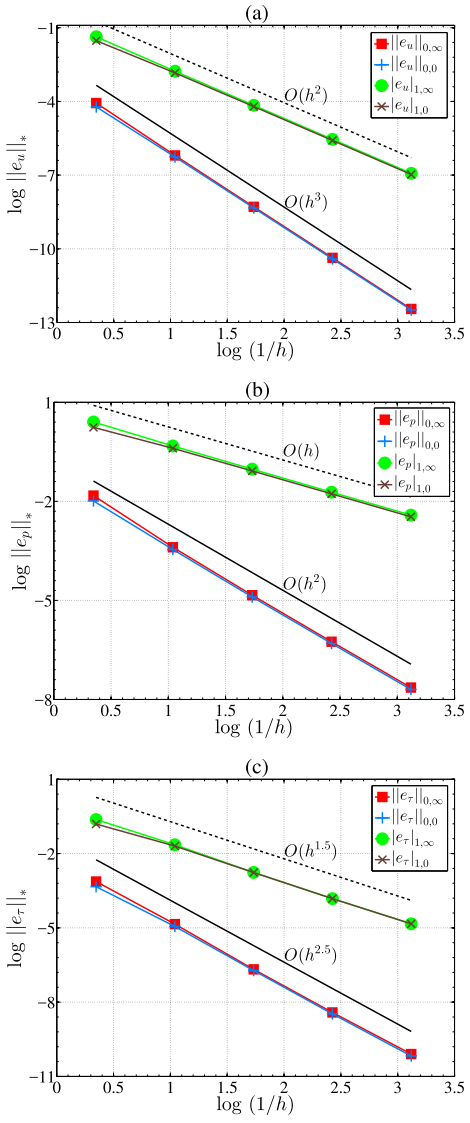


**Fig. 4.** Convergence test for (a) velocity, (b) pressure and (c) viscoelastic conformation stress fields.

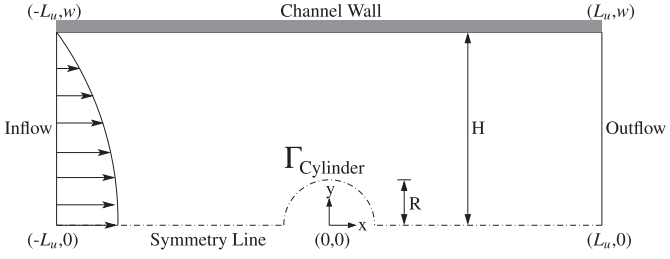


**Fig. 5.** Schematic representation of flow past a cylinder in a rectangular channel.

Find $(\mathbf{u}_h^{n+1}, p_h^{n+1}, \boldsymbol{\tau}_h^{n+1}) \in V_h \times Q_h \times S_h$ such that

$$\left(\frac{\mathbf{u}_{h,m}^{n+1}-\mathbf{u}_h^n}{\delta t},\mathbf{v}_h\right)+a\left(\mathbf{u}_{h,m-1}^{n+1},\mathbf{u}_{h,m}^{n+1},\mathbf{v}_h\right)-b\left(p_{h,m}^{n+1},\mathbf{v}_h\right)+c\left(\boldsymbol{\tau}_{h,m}^{n+1},\mathbf{v}_h\right)+S_1\left(\mathbf{u}_{h,m}^{n+1},\mathbf{v}_h\right)=0,$$
$$b\left(q_h,\mathbf{u}_{h,m}^{n+1}\right)=0,$$
$$\left(\frac{\boldsymbol{\tau}_{h,m}^{n+1}-\boldsymbol{\tau}_h^n}{\delta t},\boldsymbol{\psi}_h\right)+e\left(\boldsymbol{\tau}_{h,m}^{n+1},\boldsymbol{\psi}_h\right)+S_2\left(\boldsymbol{\tau}_{h,m}^{n+1},\boldsymbol{\psi}_h\right)$$

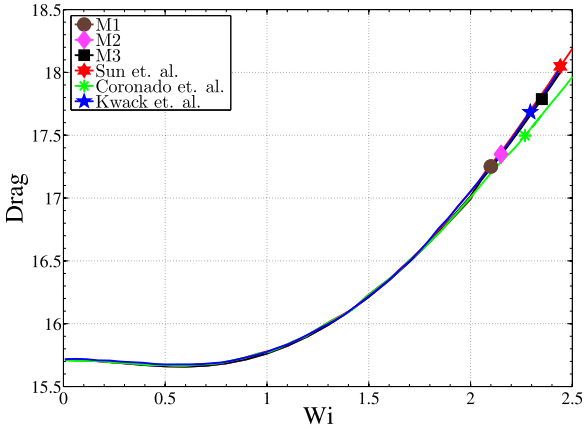


**Fig. 6.** Flow past a cylinder in a wide channel: Drag vs Weissenberg number using the three meshes M1, M2, M3 compared with results of Sun et al. [18], Coronado et al. [21] and Kwack et al. [26].

$$+ d\left(\mathbf{u}_{h,m-1}^{n+1}, \boldsymbol{\tau}_{h,m}^{n+1}, \boldsymbol{\psi}_h\right) + d\left(\mathbf{u}_{h,m}^{n+1}, \boldsymbol{\tau}_{h,m-1}^{n+1}, \boldsymbol{\psi}_h\right) - d\left(\mathbf{u}_{h,m-1}^{n+1}, \boldsymbol{\tau}_{h,m-1}^{n+1}, \boldsymbol{\psi}_h\right) = f\left(\boldsymbol{\psi}_h\right), \tag{15}$$

for $1 \le m \le \mathrm{M}$ and $(\mathbf{v}_h, q_h, \boldsymbol{\psi}_h) \in V_{h,0} \times Q_h \times S_h$. We refer to [51] for the details on assembling of matrices in the Navier–Stokes system.

**Remark 1.** Note that the stabilizing terms $S_1$ and $S_2$ are linear. Hence, it is enough to assemble these terms only once at the beginning of the computations, which is very efficient compared to the state-of-the-art residual based methods where the stabilization matrices need to be assembled not only at every time step but also at each nonlinear iteration step.

The linearized system of algebraic equations (15) are solved using the Multifrontal Massively Parallel Sparse (MUMPS) direct solver [52,53]. Here, we follow a monolithic approach to solve for the velocity, pressure and conformation stress variables. The proposed numerical scheme for viscoelastic fluid flows is implemented in our in-house finite element code ParMooN [54,55].

## 4. Numerical results

In this section we present the numerical results of Oldroyd-B viscoelastic fluid flows obtained by the proposed one-level LPS scheme. A convergence study using the method of manufactured solutions is first presented for the proposed scheme. We then present the numerical results for a stationary viscoelastic flow over a cylinder in a rectangular channel and a time-dependent viscoelastic lid-driven cavity flow. The numerical results are compared with the corresponding results in the literature and the effects of Weissenberg number on the flow dynamics are examined for inertial and non-inertial flows.

### 4.1. Convergence test

In this section, we present a convergence study of the proposed one-level local projection stabilized formulation for computations of Oldroyd-B viscoelastic fluid flows. Force terms are introduced in the Navier–Stokes and the conformation stress tensor equations (7) such that the exact solution satisfies

$$\begin{aligned} u_x(x,y) &= \exp(-0.1t)\sin(\pi x),\\ u_y(x,y) &= -\pi\exp(-0.1t)y\cos(\pi x),\\ p(x,y) &= \exp(-0.1t)\sin(\pi x)\cos(\pi y),\\ \tau_{xx}(x,y) &= \exp(-0.1t)\sin(\pi x),\\ \tau_{xy}(x,y) &= -\pi\exp(-0.1t)y\cos(\pi x),\\ \tau_{yy}(x,y) &= \exp(-0.1t)\sin(\pi x)\cos(\pi y). \end{aligned}$$

Further, the initial and non-homogeneous Dirichlet boundary values are chosen from the above exact solution. The computational domain is a unit square $[0, 1]^2$. The computations are performed using quadrilateral meshes which are obtained by successive uniform refinement of the initial coarse mesh. The coarsest mesh used in this convergence study consists of four cells as depicted in Fig. 3. In each mesh level, we solved the problem with $\mathrm{Re} = 0.5$, $\mathrm{Wi} = 0.25$, $\beta = 0.75$, $\delta t = h^2$, $c_1 = 0.1$, $c_2 = 0.1$ and $c_3 = 0.05$. Further, the finite element spaces for velocity / pressure / conformation stress tensor are chosen to be $Q_2^{bubble}$ / $P_1^{disc}$ / $Q_2^{bubble}$. We evaluate the discretization errors in the velocity, pressure and viscoelastic conformation stress fields in space with $L^2$ – norm and $H^1$ – semi-norm, and in time with $l^\infty$ – norm and $l^2$ – norm, i.e.,

$$\begin{aligned} \|e_{\mathbf{u}}\|_{0,\infty} &:= \sup_{n=1,2,\ldots N} \|\mathbf{u}(\mathbf{x},t^n) - \mathbf{u}_h(\mathbf{x},t^n)\|_{L^2(\Omega)}\\ \|e_{\mathbf{u}}\|_{0,0} &:= \left(\int_0^T \|\mathbf{u}(\mathbf{x},t^n) - \mathbf{u}_h(\mathbf{x},t^n)\|_{L^2(\Omega)}^2 dt\right)^{1/2}\\ |e_{\mathbf{u}}|_{1,\infty} &:= \sup_{n=1,2,\ldots N} |\mathbf{u}(\mathbf{x},t^n) - \mathbf{u}_h(\mathbf{x},t^n)|_{H^1(\Omega)}\\ |e_{\mathbf{u}}|_{1,0} &:= \left(\int_0^T |\mathbf{u}(\mathbf{x},t^n) - \mathbf{u}_h(\mathbf{x},t^n)|_{H^1(\Omega)}^2 dt\right)^{1/2}. \end{aligned}$$

Suppose $r$ is the polynomial order of the finite element basis function, then the optimal order of convergence for the velocity and pressure in $L^2$ – norm and in $H^1$ – semi-norm are of the order $r+1$ and $r$, respectively, whereas the optimal order of convergence for the viscoelastic conformation stress in $L^2$ – norm and in $H^1$ – semi-norm are expected to be $r+1/2$ and $r-1/2$ respectively, refer [56] for error estimates of transient convection-diffusion-reaction problems with Local Projection Stabilization. Fig. 4 shows the computed errors in the velocity, pressure and viscoelastic conformation stress fields in the respective norms at each mesh level. We can observe the optimal order of convergence for the velocity, pressure and viscoelastic conformation stress in the respective norms.

### 4.2. Flow past a cylinder in a rectangular channel

The flow of an Oldroyd-B fluid past a cylinder in a rectangular channel is a standard benchmark problem to validate the computational methods for viscoelastic fluids [9,18,20,21,26,35–37]. Fig. 5 shows the schematic representation of the computational domain. Due to the symmetry of the problem along the x-axis, we consider only the upper half of the channel to reduce the computational cost. At the inflow, we impose a fully developed parabolic velocity profile

$$u_x = 1.5\left(1 - \frac{y^2}{w^2}\right), \quad u_y = 0,$$

where $w$ is the half of the channel width. Further, we set the viscoelastic conformation stress tensor components at the inflow boundary to the steady state solution of the Poiseuille flow of an Oldroyd-B fluid, which is given by

$$\tau_{xx} = 1 + 2\left(\mathrm{Wi}\frac{\partial u_x}{\partial y}\right)^2, \quad \tau_{xy} = \mathrm{Wi}\frac{\partial u_x}{\partial y}, \quad \tau_{yy} = 1.$$

On the channel wall and cylinder surface, we impose the no-slip boundary condition, i.e. $\mathbf{u} = 0$, and along the symmetry line, $y = 0$, we impose the free slip boundary condition, i.e.,

$$u_y = 0, \quad \mathbf{n}\cdot\mathbb{T}(\mathbf{u}, p, \boldsymbol{\tau}) = 0,$$

where $\mathbf{n}$ is the unit outward normal vector on the symmetric line and on the cylinder. To generate a triangular mesh, we use the Triangle [57,58] package, which is based on constrained Delaunay triangulation and the constraint we impose is the number of vertices

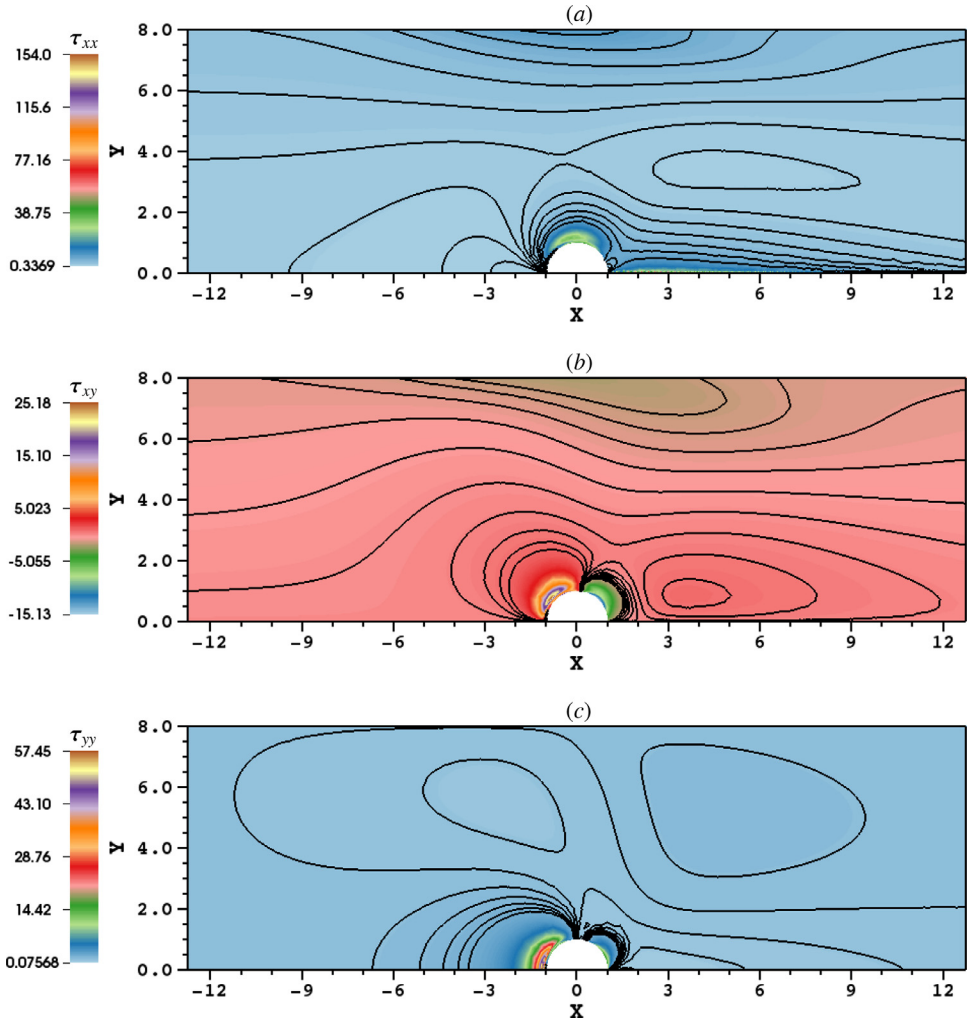


**Fig. 7.** Contour plots for flow past a cylinder in a wide channel: (a) $\tau_{xx}$, (b) $\tau_{xy}$ and (c) $\tau_{yy}$ profiles at Wi = 2.45 on the mesh M3.

on each boundary and maximum area of each cell in the computational domain. Further, we specify a relatively higher number of vertices along the symmetry line and on the cylinder in order to obtain very fine mesh to capture the high gradients in the viscoelastic conformation stresses. The finite element spaces for the velocity / pressure / viscoelastic conformation stress tensor are chosen as $P_2^{bubble}$ / $P_1^{disc}$ / $P_2^{bubble}$. Further, we compute the steady-state solution, i.e. we neglect the time derivative terms in both the momentum and in the Oldroyd-B constitutive equations. Traditionally, the drag force on the cylinder is used to compare the computational results of flow past a cylinder, which is defined as follows:

$$F_d = 2\int_{\Gamma_{Cylinder}} \mathbf{n}\cdot\mathbb{T}(\mathbf{u},p,\boldsymbol{\tau})\cdot(1,0)^{\mathrm{T}}\,ds, \tag{16}$$

where the multiplication by 2 is due to the half-domain configuration. Nevertheless, the drag force over $\Gamma_{Cylinder}$ is calculated using volume integral formulations as described in [59], instead of approximating the surface integral in (16).

*4.2.1. Flow in a wide channel*

In this section, we consider a 2D planar viscoelastic flow past a cylinder in a wide channel with R = 1, H = 8, $L_u$ = 40 and $w$ = 8. Table 1 presents the data of the three triangular meshes used in this study. Further, the constants used in computations are $\beta$ = 0.59, $c_1$ = 0.1, $c_2$ = 0.1 and $c_3$ = 0.05. We study the effects of viscoelasticity on the flow dynamics for inertial and non-inertial flows.

**Table 1**
Flow past a cylinder in a wide channel: characteristics of triangular meshes.

| Mesh | Cells | $h_{min}$ | DOFs |
|---|---|---|---|
| M1 | 15,936 | 0.0435 | 454,513 |
| M2 | 23,399 | 0.0323 | 667,362 |
| M3 | 32,702 | 0.0257 | 931,721 |

*4.2.1.1. Non-inertial flow.* The convective velocity term in the momentum equation is neglected in computations in order to benchmark our results with those in the literature. The computed values of the drag force on the cylinder with different Weissenberg numbers using the meshes M1, M2 and M3 are plotted in Fig. 6 and compared with the results of Sun et al. [18], Coronado et al. [21] and Kwack et al. [26]. The maximum achievable Weissenberg number in computations is 2.45, beyond which the numerical solutions did not converge due to the large gradients in the viscoelastic conformation stresses. A complete overlap of drag predictions from these three meshes is observed across all Weissenberg numbers. Further, an excellent agreement with the results in the literature till Wi = 2.0 with a maximum relative difference of 0.2% is obtained. Beyond Wi = 2.0, the drag values are in good

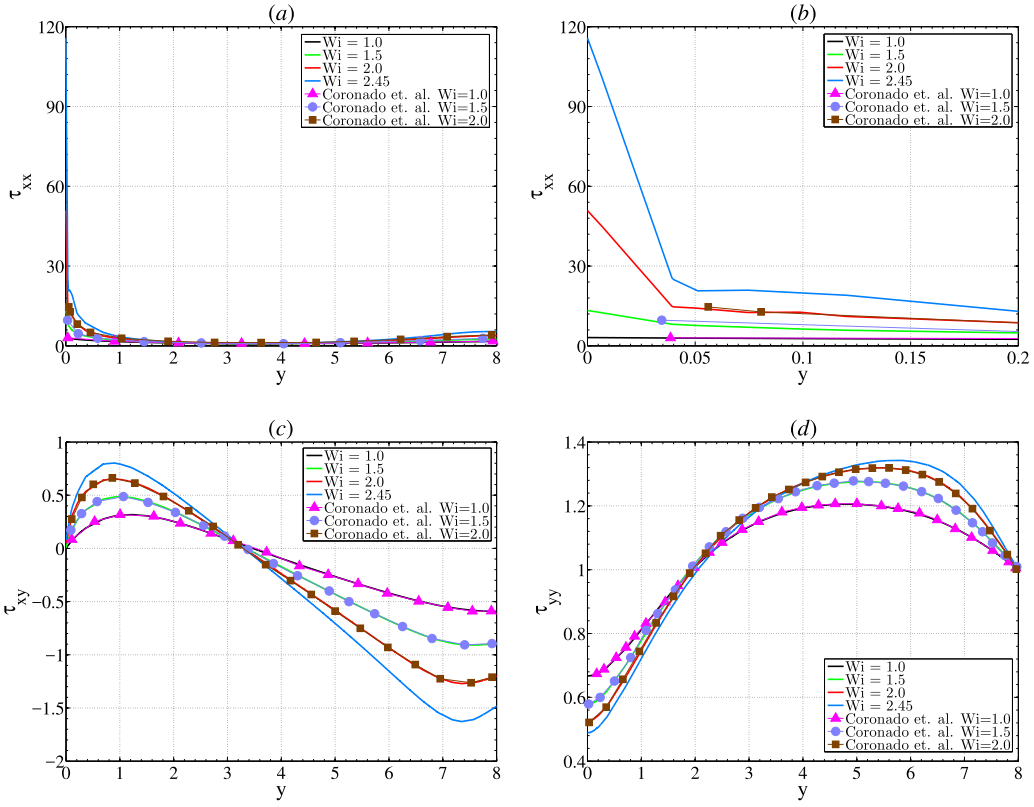


**Fig. 8.** Flow past a cylinder in a wide channel: (a) $\tau_{xx}$, (b) magnified view of $\tau_{xx}$, (c) $\tau_{xy}$ and (d) $\tau_{yy}$ along the line x = 4 on the mesh M3 and different Weissenberg numbers.

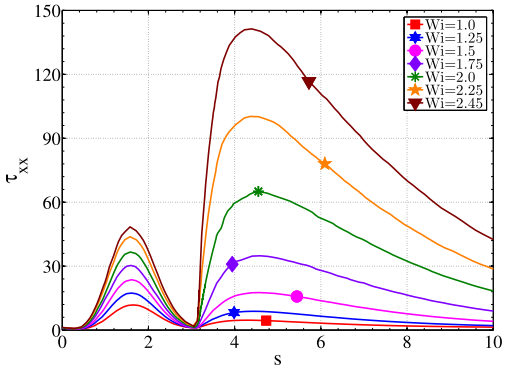


**Fig. 9.** Flow past a cylinder in a wide channel: $\tau_{xx}$ on the cylinder and along the symmetry line with various Weissenberg numbers on the mesh M3.

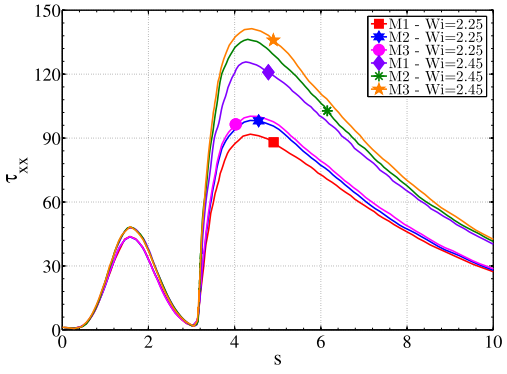


**Fig. 10.** Flow past a cylinder in a wide channel: $\tau_{xx}$ on the cylinder and along the symmetry line with Wi = 2.25 and Wi = 2.45 on different meshes M1, M2 and M3.

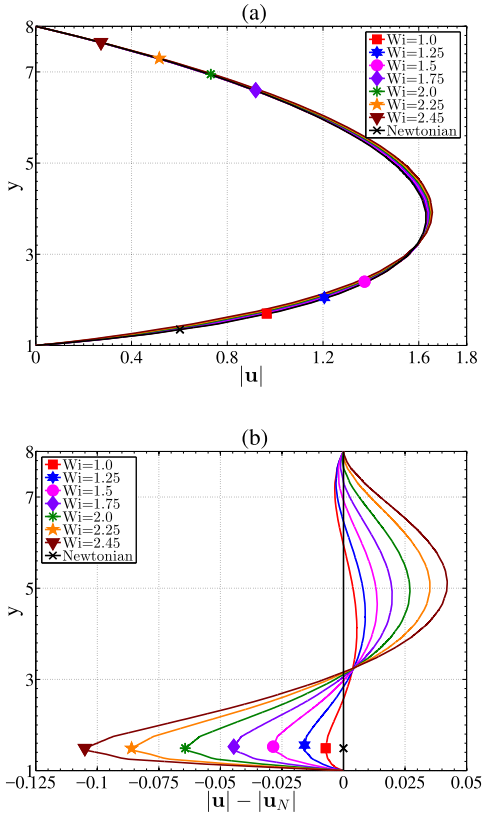


**Fig. 11.** Flow past a cylinder in a wide channel: Dependence of (a) $|\mathbf{u}|$ and (b) $|\mathbf{u}| - |\mathbf{u}_N|$ on Weissenberg number along x = 0.

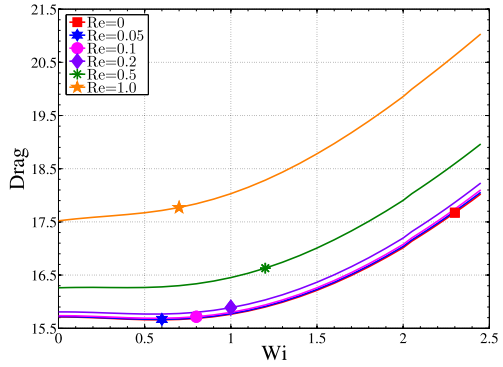


**Fig. 12.** Flow past a cylinder in a wide channel: Drag vs Weissenberg number with different Reynolds numbers.

agreement with Sun et al. [18] and Kwack et al. [26]. However, the results of Coronado et al. [21] under-predict the drag values beyond Wi = 2.0, with maximum relative difference compared to our results being 0.9% at Wi = 2.45.

Fig. 7 displays the contour plots of the components of viscoelastic conformation stress tensor at Wi = 2.45. Fig. 7(a) shows steep gradients in $\tau_{xx}$ on top of the cylinder and in the wake region. The gradient in $\tau_{xx}$ increases with an increase in the Weissenberg number. Sharp boundary layers exist in conformation stress component $\tau_{xx}$ in the wake region, which is the source of breakdown in convergence of numerical simulations at high Weissenberg numbers. High gradient in the conformation stress component $\tau_{xy}$ (Fig. 7(b)) is observed along the circumference of the cylinder. Further, we also observe high gradients in the conformation stress component $\tau_{yy}$ near the stagnation points of the cylinder, see Fig. 7(c). Note that the gradient of the stress component $\tau_{yy}$ is higher at the front stagnation point.

Fig. 8 presents the line plots of the variation of components of the viscoelastic conformation stress tensor versus the depth of the channel along the cross-section x = 4 for Wi = 1.0, 1.5, 2.0 and 2.45. Further, our results are in excellent agreement with Coronado et al. [21] with a maximum relative difference of 0.947%, 0.378% and 0.426% in $\tau_{xx}$, $\tau_{xy}$ and $\tau_{yy}$ plots, respectively. From Fig. 8(b), we can observe a steep gradient in the conformation stress component $\tau_{xx}$ close to the symmetry line. Further, closer to x = 0 the values of $\tau_{xx}$ increases with an increase in the Weissenberg number. From Fig. 8(c) and (d), we can observe that the Weissenberg number has a significant effect on $\tau_{xy}$ and $\tau_{yy}$ in the wake region throughout the depth of the channel.

Fig. 9 shows the plot of $\tau_{xx}$ versus $s$ with various Weissenberg numbers, where $0 < s < \pi R$ is defined as the perimeter of the cylinder and in the wake along the symmetry line ($s = x + \pi R - R$) when $s > \pi R$. We can observe that two peaks exist in the curves of $\tau_{xx}$. One, on the top of the cylinder and the other in the wake region. The peaks also increase with an increase in the Weissenberg number. However, the effect of increase in $\tau_{xx}$ with Weissenberg number is larger in the wake region than on the top of the cylinder. Further, we can observe that the maximum value in $\tau_{xx}$ is higher in the wake region when Wi $\gtrsim$ 1.75, whereas the maximum value in $\tau_{xx}$ is higher on the top of the cylinder when Wi $\lesssim$ 1.75. This effect is due to the dominance of the viscous force over the elastic force, when Wi is small. At high Weissenberg numbers, the viscoelastic stress profiles depend on the mesh resolution in the wake region. Fig. 10 addresses this mesh dependence for Wi = 2.25 and 2.45. We can observe that with finer meshes, we get converged solutions.

Next, Fig. 11(a) presents the magnitude of the velocity versus the depth of the channel along the cross-section from the top of

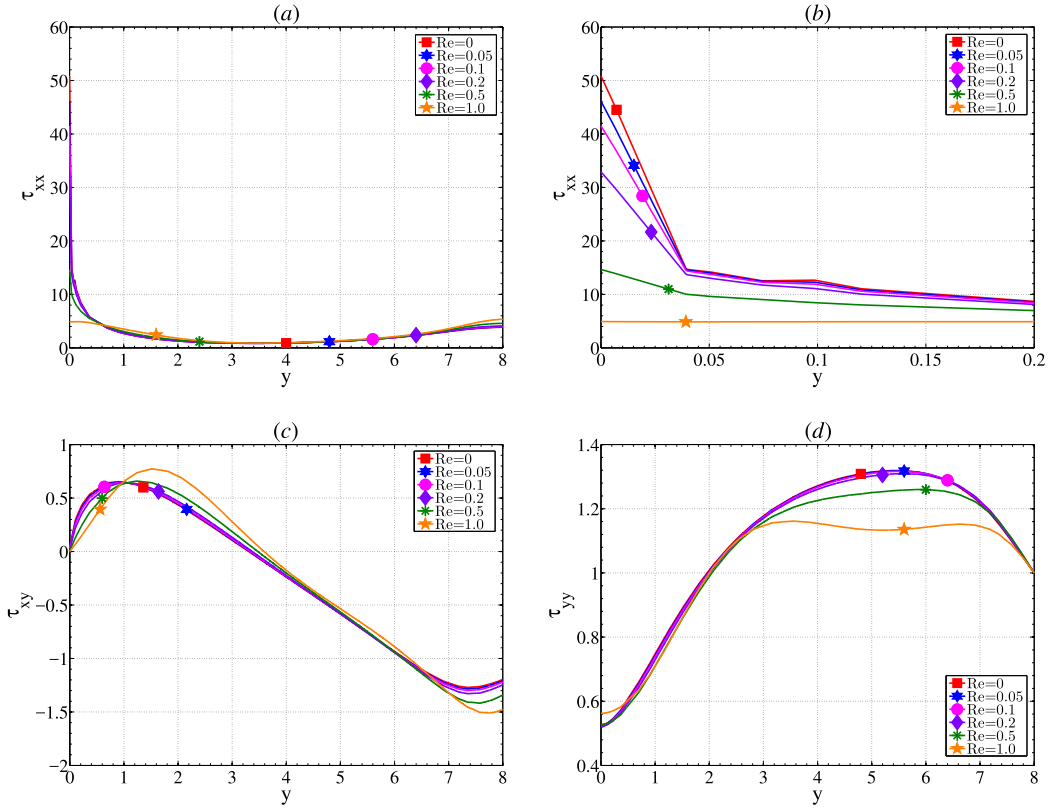


**Fig. 13.** Flow past a cylinder in a wide channel: (a) $\tau_{xx}$, (b) magnified view of $\tau_{xx}$, (c) $\tau_{xy}$ and (d) $\tau_{yy}$ along the line x = 4 at Wi = 2.0 and different Reynolds numbers on the mesh M3.

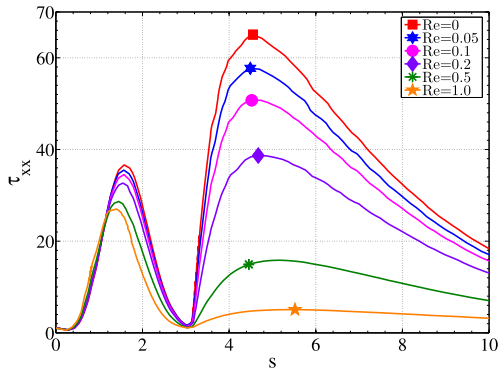


**Fig. 14.** Flow past a cylinder in a wide channel: $\tau_{xx}$ on the cylinder and along the symmetry line at Wi = 2.0 and different Reynolds numbers on the mesh M3.

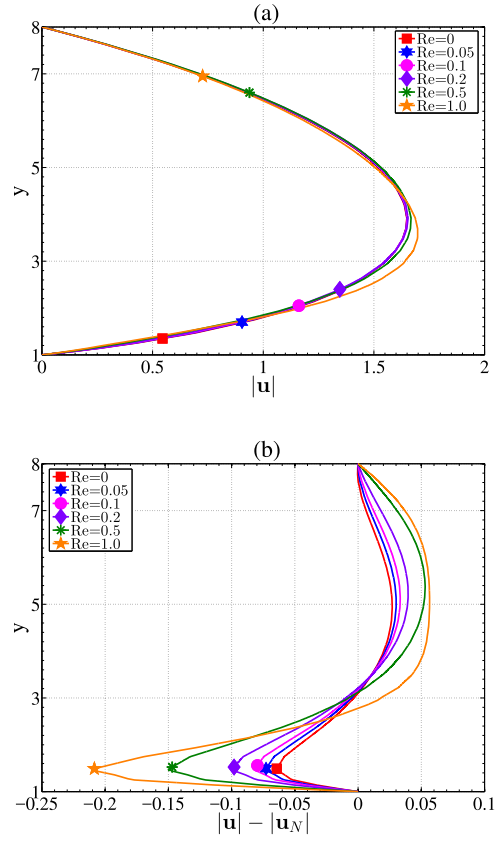


**Fig. 15.** Flow past a cylinder in a wide channel: Dependence of (a) $|\mathbf{u}|$ and (b) $|\mathbf{u}| - |\mathbf{u}_N|$ on Reynolds number with Wi = 2.0 along x = 0.

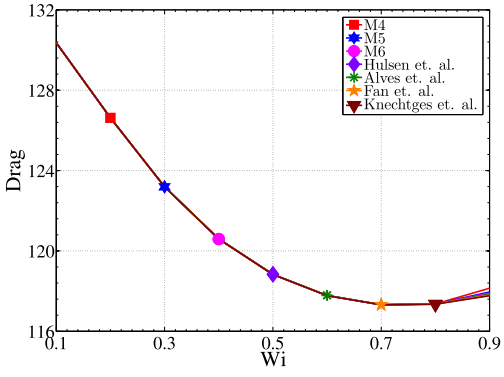


**Fig. 16.** Flow past a cylinder in a narrow channel: Drag vs Weissenberg number using the three meshes M4, M5 and M6 compared with results of Hulsen et al. [36], Alves et al. [35], Fan et al. [20] and Knechtges et al. [9].

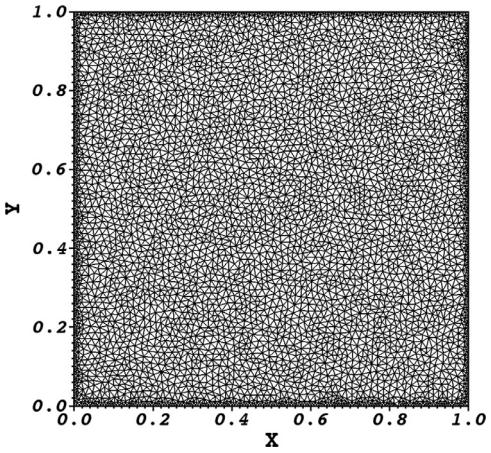


**Fig. 17.** Unstructured triangular mesh (M7) used in lid-driven cavity example.

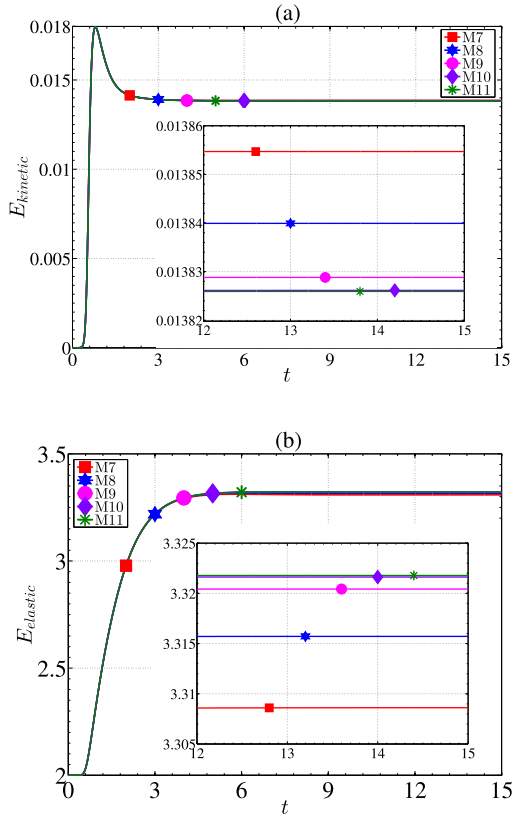


**Fig. 18.** Grid independence test for lid-driven cavity flow: evolution of average (a) kinetic and (b) elastic energies at Wi = 0.5.

the cylinder to the channel wall, i.e., along the line x = 0. The velocity is reduced near the cylinder in comparison to the parabolic Newtonian flow profile, whereas the velocity increases near the middle region between the cylinder and the wall. The magnitude of the effect of Weissenberg number on the velocity in comparison with the Newtonian velocity ($\mathbf{u}_N$) profile is plotted in Fig. 11(b). We can observe that the magnitude of peaks increases with an increase in the Weissenberg number.

*4.2.1.2. Inertial flow.* In this section, we investigate the effects of inertia on the viscoelastic fluid flow past a cylinder in a wide channel. The computed drag values for Re = 0, 0.05, 0.1, 0.2, 0.5 and

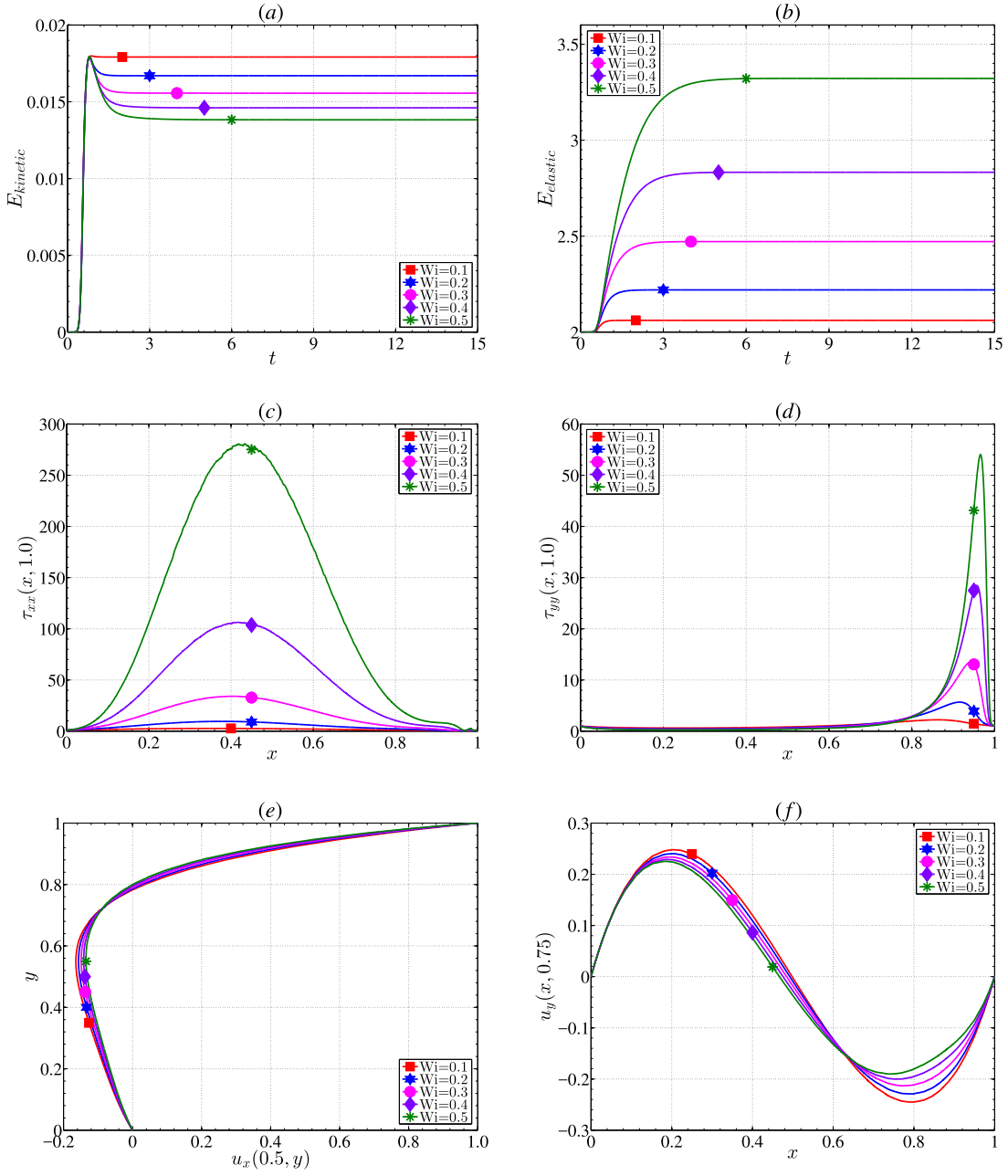


**Fig. 19.** Lid-driven cavity flow: Numerical solutions of the profiles of (a) kinetic energy versus time, (b) elastic energy versus time, (c) cross-section of $\tau_{xx}$ versus x along $y = 1$, (d) cross-section of $\tau_{yy}$ versus x along $y = 1$, (e) cross-section of $u_x$ versus y along $x = 0.5$ and (f) cross-section of $u_y$ versus x along $y = 0.75$ at different Weissenberg numbers.

1.0 with various Weissenberg numbers are plotted in Fig. 12. For a given Weissenberg number, we can observe that the drag values increase with an increase in the Reynolds number. In order to perform a quantitative assessment of the effects of inertia on the drag values, the minimum and maximum relative difference in the drag values across the range of computed Weissenberg numbers for each Reynolds number are tabulated in Table 2 using:

$$\delta_{min}\Big|_{\mathrm{Re}} = \min_{\mathrm{Wi}\in[0,2.45]} \left| \frac{F_d\Big|_{\mathrm{Re}}^{\mathrm{Wi}} - F_d\Big|_{\mathrm{Re=0}}^{\mathrm{Wi}}}{F_d\Big|_{\mathrm{Re=0}}^{\mathrm{Wi}}} \right| \times 100\,\%,$$

**Table 2**
Flow past a cylinder in a wide channel: Percentage minimum/maximum relative difference in the drag values due to inertia.

| Re | $\delta_{min}$(%) | $\delta_{max}$(%) |
|---|---|---|
| 0.05 | 0.0380 | 0.1836 |
| 0.1 | 0.1517 | 0.4290 |
| 0.2 | 0.5999 | 1.1385 |
| 0.5 | 3.4852 | 5.2288 |
| 1.0 | 11.5034 | 16.7251 |

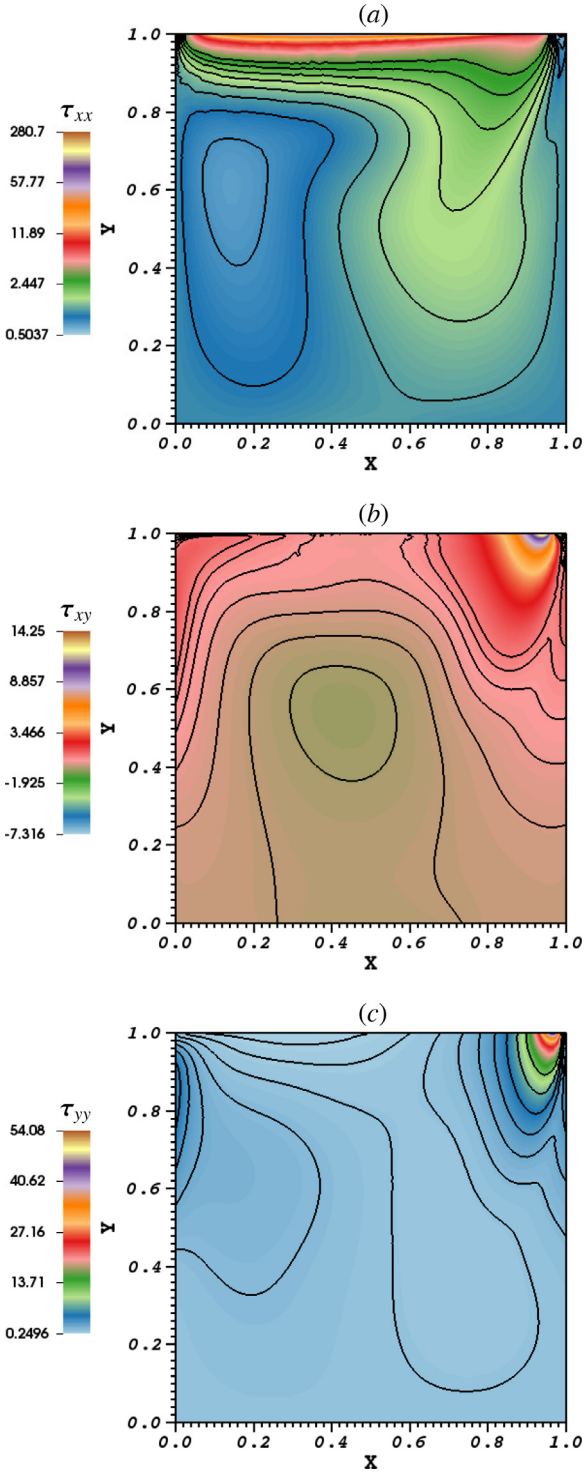


**Fig. 20.** Lid-driven cavity flow: Contour plots of (a) $\tau_{xx}$, (b) $\tau_{xy}$ and (c) $\tau_{yy}$ with Wi = 0.5 at the steady state.

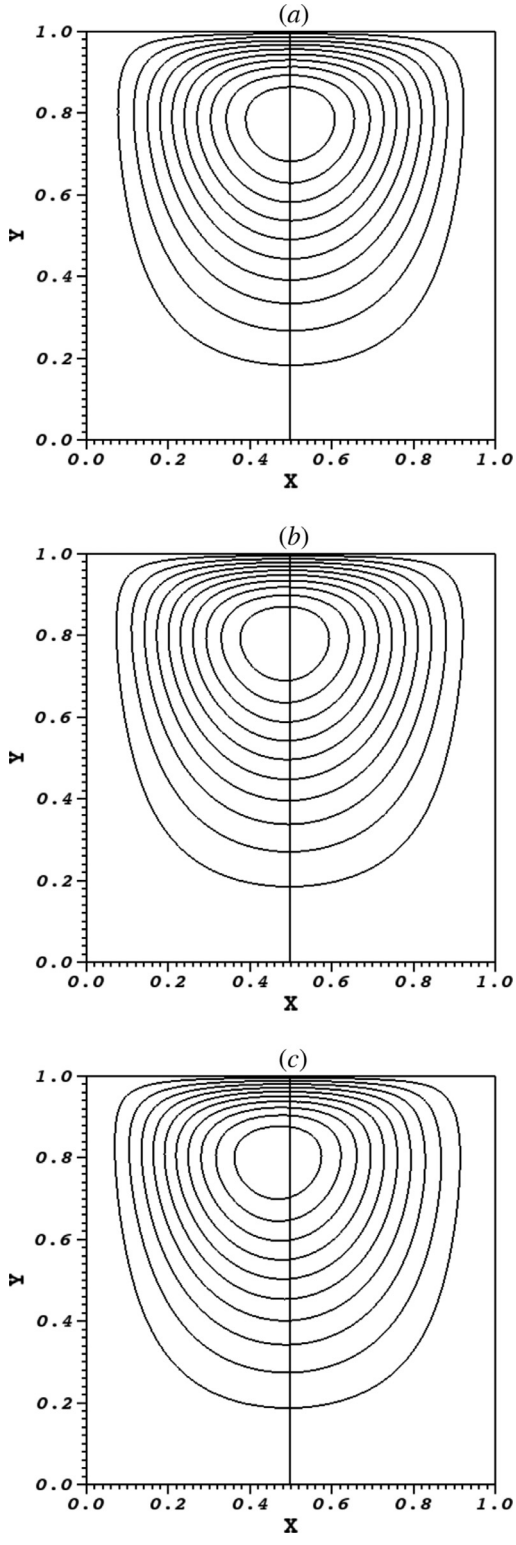


**Fig. 21.** Lid-driven cavity flow: Streamline patterns with (a) Wi = 0.1, (b) Wi = 0.3 and (c) Wi = 0.5 at the steady state.

$$\delta_{max}\Big|_{\mathrm{Re}} = \max_{\mathrm{Wi}\in[0,2.45]} \left| \frac{F_d\Big|_{\mathrm{Re}}^{\mathrm{Wi}} - F_d\Big|_{\mathrm{Re}=0}^{\mathrm{Wi}}}{F_d\Big|_{\mathrm{Re}=0}^{\mathrm{Wi}}} \right| \times 100\,\%.$$

Here, the superscripts and subscripts over the drag force $F_d$ denote that the drag values are obtained with the respective Weissenberg and Reynolds numbers. Since the effects of inertia increases monotonically with an increase in the Reynolds number, $\delta_{\min}$ and $\delta_{\max}$ values also increase.

Fig. 13 presents the line plots of the variation of components of the viscoelastic conformation stress tensor versus the depth of the channel along the cross-section x = 4 at Wi = 2.0 with varying Reynolds number. From Fig. 13(b), we can observe a steep gradient of the conformation stress component $\tau_{xx}$ in the vicinity of

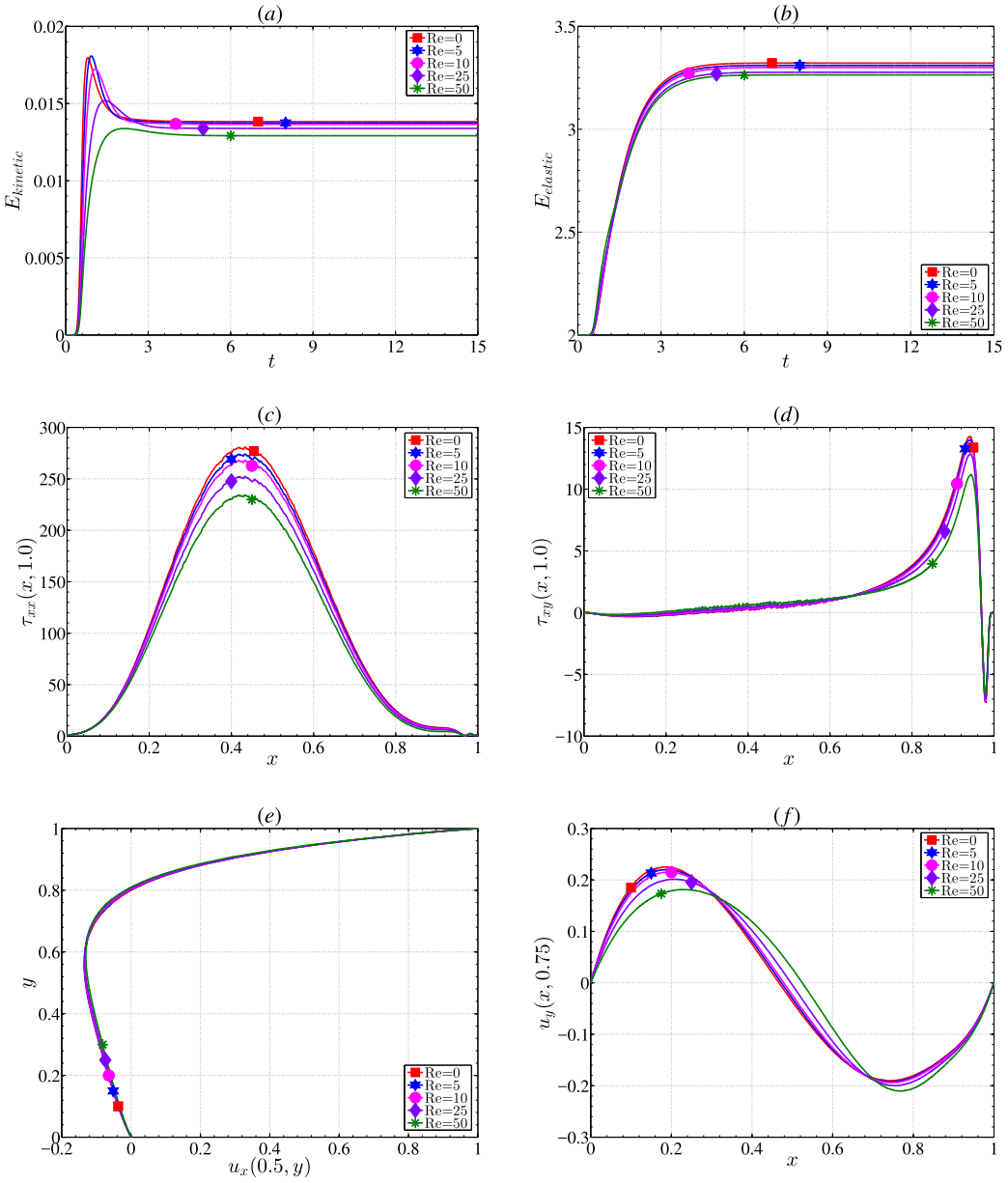


**Fig. 22.** Lid-driven cavity flow: Numerical solutions of the profiles of (a) kinetic energy versus time, (b) elastic energy versus time, (c) cross-section of $\tau_{xx}$ versus x along $y = 1$, (d) cross-section of $\tau_{xy}$ versus x along $y = 1$, (e) cross-section of $u_x$ versus y along $x = 0.5$ and (f) cross-section of $u_y$ versus x along $y = 0.75$ at Wi = 0.5 and different Reynolds numbers.

the symmetry line. Further, closer to x = 0 the values of $\tau_{xx}$ decreases while increasing Reynolds number, which suggests that the inertial forces counter the forces due to viscoelastic stresses along the symmetry line. We can also observe that the Reynolds number has a significant effect on $\tau_{xy}$ closer to the symmetric line and the channel wall. However, the effects of Reynolds number on $\tau_{yy}$ are observed in the middle region between the symmetric line and the channel wall.

Fig. 14 shows the variation of $\tau_{xx}$ over the surface of the cylinder and over the wake region of the channel at Wi = 2.0 and different Reynolds numbers. The values of $\tau_{xx}$ decreases with an increase in the Reynolds number. Nevertheless, the decrease at the top of the cylinder is very less. However, $\tau_{xx}$ values decrease strongly in the wake region of the cylinder with an increase in the Reynolds number. Further, we can observe that $\tau_{xx}$ values are higher in the wake region when Re $\lesssim$ 0.2 and higher on top of the cylinder when Re $\gtrsim$ 0.2.

Oscillations in the computed values of the conformation stresses are observed in the wake region of the flow at low Reynolds numbers, see Fig. 14. It could be due to a non-optimal choice of the stabilization parameter or due to failure of the low order basis functions to capture exponentially growing stress profiles. Identifying an optimal choice of local stabilization parameter is very challenging. Further, the oscillations could be suppressed by improving the proposed numerical scheme using the log-conformation representation of the conformation tensor [8,9].

Fig. 15(a) presents the magnitude of velocity versus the depth of the channel along the cross-section from top of the cylinder to the channel wall, i.e., along the line x = 0 with Wi = 2.0 and different values of Reynolds numbers. The velocity is reduced near the cylinder in comparison to the parabolic Newtonian flow profile, whereas the velocity increases in the middle region between the cylinder and the wall. The magnitude of the effects of Reynolds number on the velocity in comparison with the Newtonian flow

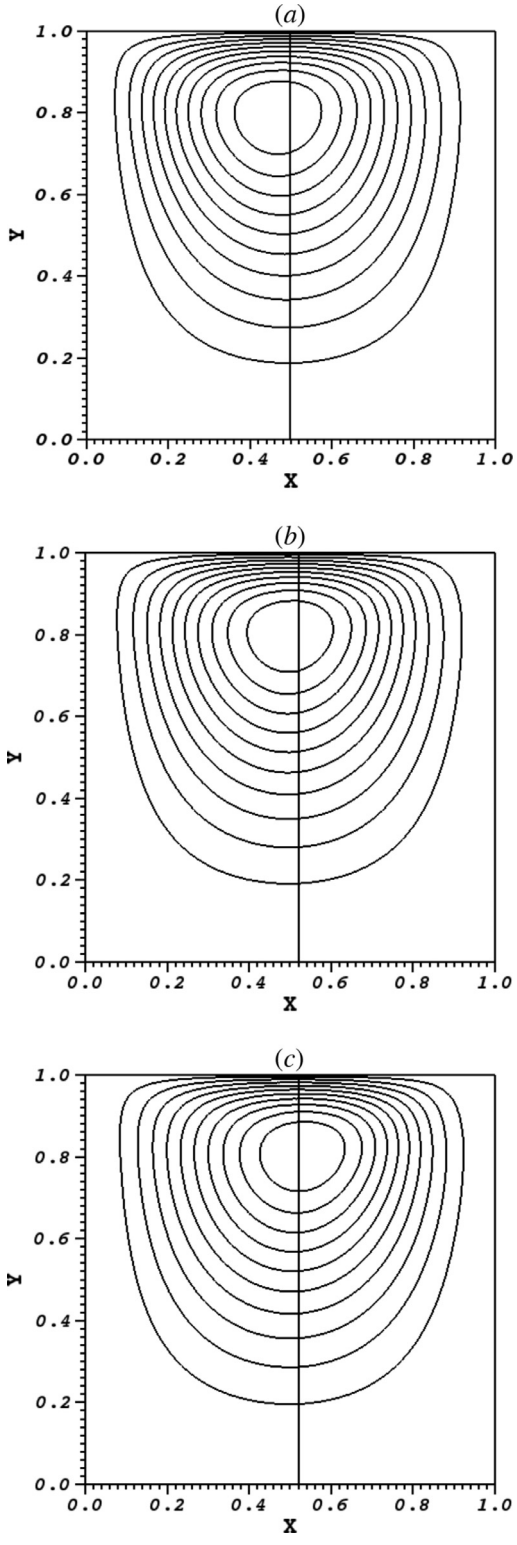


**Fig. 23.** Lid-driven cavity flow: Streamline patterns with Wi = 0.5 and (a) Re = 0, (b) Re = 25 and (c) Re = 50 at the steady state.

profile is plotted in Fig. 15(b). We can observe that the magnitude of peaks increases with an increase in the Reynolds number.

#### 4.2.2. Flow in a narrow channel

In this section, we consider a 2D planar viscoelastic flow past a cylinder in a narrow channel with R = 1, H = 2, $L_u = 15$ and $w = 2$. Table 3 presents the data of the three triangular meshes used in this study. Further, the constants used in computations are $\beta = 0.59$, $c_1 = 0.01$, $c_2 = 0.005$ and $c_3 = 0.005$. The convective velocity term in the momentum equation is neglected in computations in order to benchmark our results with those in the literature. The computed values of the drag force on the cylinder with different Weissenberg numbers using the meshes M4, M5 and M6 are plotted in Fig. 16 and compared with the results of Hulsen et al. [36], Alves et al. [35], Fan et al. [20] and Knechtges et al. [9]. The maximum achievable Weissenberg number in computations is 0.9, beyond which the numerical solutions did not converge due to the large gradients in the viscoelastic conformation stresses. A complete overlap of drag predictions from these three meshes is observed across all Weissenberg numbers till Wi = 0.8. Further, excellent agreement with the results in the literature with a maximum relative difference of 0.112% is obtained.

**Table 3**
Flow past a cylinder in a narrow channel: characteristics of triangular meshes.

| Mesh | Cells | $h_{\min}$ | DOFs |
|---|---|---|---|
| M4 | 18,750 | 0.0127 | 534,175 |
| M5 | 25,162 | 0.0106 | 715,461 |
| M6 | 33,104 | 0.0079 | 941,347 |

### 4.3. Lid-driven cavity flow

In this section, we consider the flow of an Oldroyd-B fluid in a lid-driven cavity, which is one of the standard test problems for validation of numerical schemes for computations of viscoelastic fluid flows [8,37–42]. The fluid is confined in a unit square $[0, 1]^2$ domain, bounded by solid walls with the top boundary moving to the right. Unlike Newtonian fluids, viscoelastic fluids cannot sustain deformations near the upper corners and therefore the motion of the lid needs to be regularized such that $\nabla \mathbf{u}$ vanishes at the corners [8]. Accordingly, the velocity of the lid is taken as:

$$u_x(x,t) = 8[1+\tanh(8(t-0.5))]x^2(1-x)^2, \quad u_y(x,t) = 0.$$

This choice of velocity provides a smooth start and for $t > 0.5$, the lid velocity attains its maximum $\mathbf{u} = (1,0)^{\mathrm{T}}$ at the middle, $x = 0.5$ of the top boundary. On all other walls, we impose the no-slip boundary condition for the velocity. Further, the initial condition for the velocity is taken as $\mathbf{u} = (0,0)^{\mathrm{T}}$ and for the conformation stress we impose $\boldsymbol{\tau} = \mathbb{I}$. The dimensionless constants used in computations are $\beta = 0.5$, $c_1 = 0.1$, $c_2 = 0.1$ and $c_3 = 0.05$. Further, the finite element spaces for velocity / pressure / conformation stress tensor are $P_2^{bubble}$ / $P_1^{disc}$ / $P_2^{bubble}$. To quantitatively analyze the rheological behaviour of Oldroyd-B fluids, the average kinetic and elastic energies are calculated as follows [38]:

$$E_{kinetic}(t) = \frac{1}{2}\int_\Omega |\mathbf{u}(\mathbf{x},t)|^2\, dx,$$

$$E_{elastic}(t) = \int_\Omega tr(\boldsymbol{\tau}(\mathbf{x},t))\, dx,$$

where *tr* denotes the trace of the tensor.

#### 4.3.1. Grid independence test

The unit square domain is decomposed into unstructured triangular grids using the mesh generator Triangle [57,58]. In order to identify a grid that provides a grid independent solution, we consider five different meshes of varying mesh sizes. The characteristics of these meshes are tabulated in Table 4. Fig. 17 depicts the schematic representation of the mesh M7. It has to be noted that we use an adaptive mesh with more cells near the boundaries of the cavity. We consider the average kinetic and elastic energies to study the mesh influence on the numerical solutions.

**Table 4**
Lid-driven Cavity flow: characteristics of triangular meshes.

| Mesh | Cells | $h_{min}$ | DOFs |
|---|---|---|---|
| M7 | 9514 | 0.00667 | 269,397 |
| M8 | 10,700 | 0.005 | 303,605 |
| M9 | 11,880 | 0.004 | 337,645 |
| M10 | 12,968 | 0.00333 | 369,109 |
| M11 | 14,016 | 0.002857 | 399,453 |

**Table 5**
Grid independence test for lid-driven cavity flow: Minimum value of stream function and its corresponding location at Wi = 0.5.

| Mesh | $\psi_{min}$ | $x_{min}$ | $y_{min}$ |
|---|---|---|---|
| M7 | −0.0697545 | 0.467 | 0.795 |
| M8 | −0.0697624 | 0.468 | 0.797 |
| M9 | −0.0697696 | 0.469 | 0.797 |
| M10 | −0.0697718 | 0.470 | 0.798 |
| M11 | −0.0697739 | 0.470 | 0.798 |

The time step length is set as $\delta t = 0.002$ and the computations are performed till $t = 15$, by which the flow becomes steady state. Fig. 18 depicts the convergence behaviour of the kinetic and elastic energies with different meshes for Wi = 0.5. We can observe that the flow variables gradually tend to a grid independent value when the mesh becomes finer. In particular, the numerical results obtained with the mesh M10 is quite close to those obtained with the mesh M11, which shows the grid independence of the numerical solution. Further, Table 5 lists the mesh dependence of the minimum value of the stream function and its corresponding location at Wi = 0.5. We can observe the numerical solutions to be grid independent when the mesh becomes fine. In order to have a fine balance between the computational cost and the accuracy, all numerical results in the following sections are obtained with the mesh M10.

*4.3.2. Non-inertial flow*

In this section, we study the viscoelastic flow in a lid-driven cavity without the effects of inertia for various Weissenberg numbers to benchmark our results with those in the literature, i.e. the convective velocity term in the momentum equation is neglected. Figs. 19(a) and 19(b) show the history of the average kinetic and elastic energies, respectively at different Weissenberg numbers. The kinetic energy grows as the lid accelerates, reaches a maximum at the end of acceleration and then decreases towards a steady value as the elastic energy builds up. Further, we observe that the magnitude of kinetic energy at steady state decreases with an increase in the Weissenberg number. However, Weissenberg number has no effect on the maximum value of the kinetic energy. Furthermore, the elastic energy at steady state increases significantly by increasing the Weissenberg number.

Figs. 19(c) and 19(d) show the steady state solution of $\tau_{xx}$ and $\tau_{yy}$, respectively, versus the length of the cavity along the cross-section $y = 1.0$. We can observe that the maximum value of $\tau_{xx}$ increases significantly when increasing the Weissenberg number. Similarly, the maximum value of $\tau_{yy}$ increases significantly with an increase in the Weissenberg number. Further, its location is in the close vicinity of the upper downstream corner leading to sharp boundary layers. Steady state numerical solution of the horizontal velocity component $u_x$ along the cross-section line $x = 0.5$ is shown in Fig. 19(e). As the Weissenberg number increases, the minimum value of the horizontal velocity component decreases in magnitude and its location moves closer to the lid. Fig. 19(f) displays the numerical solution of vertical velocity component $u_y$ along the cross-section line $y = 0.75$. The extreme values of vertical velocity component decreases with an increase in the Weissenberg number.

**Table 6**
Lid-driven Cavity flow: Comparison of minimum value of stream function and its corresponding location with the results in the literature for Wi = 0.5.

| Reference | $\psi_{min}$ | $x_{min}$ | $y_{min}$ |
|---|---|---|---|
| Current work - M11 | −0.0697739 | 0.470 | 0.798 |
| Pan et. al. [38] | −0.0700056 | 0.469 | 0.798 |
| Sousa et. al. [39] | −0.0697781 | 0.467 | 0.801 |
| Castillo et. al. [37] | - | 0.470 | 0.800 |
| Zhou et. al. [41] | - | 0.468 | 0.798 |

The contour plots of the three components of the viscoelastic conformation stress at the steady state with Wi = 0.5 are depicted in Fig. 20. We can observe that $\tau_{xx}$ has a thin boundary layer along the lid, whereas $\tau_{xy}$ and $\tau_{yy}$ have high gradient near the upper downstream corner. Further, Fig. 21 displays the streamline patterns with Wi = 0.1, 0.3 and 0.5 at the steady state. The lid-driven cavity flow problem without inertia leads to a symmetrical horizontal location of the vortex for a Newtonian fluid. However, due to the presence of elastic effects in viscoelastic fluid, this symmetry is progressively broken. The large normal stresses that are generated in the viscoelastic fluid as Weissenberg number increases are advected into the downstream direction leading to an increase in the flow resistance. To compensate this effect, the eye of the recirculation region progressively shifts towards the upstream direction, see Fig. 21, thus breaking the symmetry observed with Newtonian fluids. This effect is in accordance with the experimental observations in the literature [60]. Table 6 lists the minimum value of stream function and its corresponding location for Wi = 0.5. We can observe that our results agree well with those in the literature [37–39,41].

*4.3.3. Inertial flows*

In this section we study the effects of inertia (by varying the Reynolds number) on the flow of viscoelastic fluids in the lid-driven cavity at Wi = 0.5. We consider the following five variants: (i) Re = 0, (ii) Re = 5, (iii) Re = 10, (iv) Re = 25 and (v) Re = 50. Figs. 22(a) and 22(b) show the transient evolution of the average kinetic and elastic energies, respectively. We can observe that the kinetic and elastic energies at the steady state decreases with an increase in the Reynolds number. Figs. 22(c) and 22(d) show the steady state solution of $\tau_{xx}$ and $\tau_{xy}$, respectively, versus the length of the cavity along the cross-section line $y = 1.0$. We can observe that the peak values of $\tau_{xx}$ and $\tau_{xy}$ decrease with an increase in the Reynolds number. Steady state numerical solution of the horizontal velocity component $u_x$ along the cross-section line $x = 0.5$ is shown in Fig. 22(e). As the Reynolds number increases, the minimum value of the magnitude of horizontal velocity component decreases and its location moves closer to the lid. Fig. 22(f) displays the numerical solution of the vertical velocity component $u_y$ along the cross-section line $y = 0.75$. The extreme values of the vertical velocity component decreases with an increase in the Reynolds number. Fig. 23 depicts the streamline patterns for Re = 0, Re = 25 and Re = 50. We can observe that the eye of the recirculation region progressively shifts towards the downstream direction when the Reynolds number is increased, which is exactly the opposite to what we had observed when the Weissenberg number was increased in non-inertial flows.

## 5. Summary

A three-field local projection stabilized formulation for finite element computations of Oldroyd-B viscoelastic fluid flows at high Weissenberg numbers is presented. One-level LPS scheme based on

enriched approximation space and discontinuous projection space is used in the stabilized formulation. Proposed scheme is computationally efficient compared to the residual based stabilization schemes, and allows to use equal order interpolations for the velocity and the viscoelastic stress. The coupled system of Navier–Stokes and Oldroyd-B viscoelastic constitutive equations are solved in a monolithic approach. Numerical results displayed optimal convergence rates in the norms considered, showing the robustness of the stabilized scheme. The numerical scheme is validated using two benchmark problems: flow past a cylinder in a rectangular channel and lid-driven cavity flow. Further, the effects of elasticity and inertia are analyzed for benchmark problems. The comparison of numerical results with the results in the literature demonstrates that the one-level local projection stabilized formulation is on par with the state-of-the-art methods for computing viscoelastic fluid flows at high Weissenberg numbers.

## Acknowledgements

The work of Jagannath Venkatesan is supported by the Tata Consultancy Services (TCS), India through the TCS Research Scholarship Program.

## References

[1] J.G. Oldroyd, On the formulation of rheological equations of state, Proc. R. Soc. London A 200 (1063) (1950) 523–541.
[2] H. Giesekus, A simple constitutive equation for polymer fluids based on the concept of deformation-dependent tensorial mobility, J. Non-Newtonian Fluid Mech. 11 (1982) 69–109.
[3] R.B. Bird, P.J. Dotson, N.L. Johnson, Polymer solution rheology based on a finitely extensible bead-spring chain model, J. Non-Newtonian Fluid Mech. 7 (1980) 213–235.
[4] M.D. Chilcott, J.M. Rallison, Creeping flow of dilute polymer solutions past cylinders and spheres, J. Non-Newtonian Fluid Mech. 29 (1988) 381–432.
[5] N.P. Thien, R.I. Tanner, A new constitutive equation derived from network theory, J. Non-Newtonian Fluid Mech. 2 (1977) 353–365.
[6] W.M.H. Verbeeten, G.W.M. Peters, F.P.T. Baaijens, Differential constitutive equations for polymer melts: The extended Pom-Pom model, J. Rheol. 45 (4) (2001) 823–843.
[7] M.A. Hulsen, A sufficient condition for a positive definite configuration tensor in differential models, J. Non-Newtonian Fluid Mech. 38 (1) (1990) 93–100.
[8] R. Fattal, R. Kupferman, Time-dependent simulation of viscoelastic flows at high Weissenberg number using the log-conformation representation, J. Non-Newtonian Fluid Mech. 126 (2005) 23–37.
[9] P. Knechtges, M. Behr, S. Elgeti, Fully-implicit log-conformation formulation of constitutive laws, J. Non-Newtonian Fluid Mech. 214 (2014) 78–87.
[10] N. Balci, B. Thomases, M. Renardy, C.R. Doering, Symmetric factorization of the conformation tensor in viscoelastic fluid models, J. Non-Newtonian Fluid Mech. 166 (2011) 546–553.
[11] A.M. Afonso, F.T. Pinho, M.A. Alves, The kernel-conformation constitutive laws, J. Non-Newtonian Fluid Mech. 167–168 (2012) 30–37.
[12] A.N. Brooks, T.J.R. Hughes, Streamline upwind/Petrov–Galerkin formulations for convection dominated flows with particular emphasis on the incompressible Navier-Stokes equations, Comput. Methods Appl. Mech. Eng. 32 (1982) 199–259.
[13] J.M. Marchal, M.J. Crochet, A new mixed finite element for calculating viscoelastic flow, J. Non-Newtonian Fluid Mech. 26 (1) (1987) 77–114.
[14] D. Rajagopalan, R.C. Armstrong, R.A. Brown, Finite element methods for calculation of steady, viscoelastic flow using constitutive equations with a Newtonian viscosity, J. Non-Newtonian Fluid Mech. 36 (1990) 159–192.
[15] R. Guenette, M. Fortin, A new mixed finite element method for computing viscoelastic flows, J. Non-Newtonian Fluid Mech. 60 (1995) 27–52.
[16] A. Fortin, R. Gunette, R. Pierre, On the discrete EVSS method, Comput. Methods Appl. Mech. Eng. 189 (1) (2000) 121–139.
[17] D. Rajagopalan, R.C. Armstrong, R.A. Brown, Calculation of steady viscoelastic flow using a multimode Maxwell model: Application of the explicitly elliptic momentum equation (EEME) formulation, J. Non-Newtonian Fluid Mech. 36 (1990) 135–157.
[18] J. Sun, M.D. Smith, R.C. Armstrong, R.A. Brown, Finite element method for viscoelastic flows based on the discrete adaptive viscoelastic stress splitting and the discontinuous Galerkin method: DAVSS-G/DG, J. Non-Newtonian Fluid Mech. 86 (3) (1999) 281–307.
[19] M. Forin, A. Fortin, A new approach for the FEM simulation of viscoelastic flows, J. Non-Newtonian Fluid Mech. 32 (1989) 295–310.
[20] Y. Fan, R.I. Tanner, N. Phan-Thien, Galerkin/least-square finite-element methods for steady viscoelastic flows, J. Non-Newtonian Fluid Mech. 84 (1999) 233–256.
[21] O.M. Coronado, D. Arora, M. Behr, M. Pasquali, Four-field Galerkin/least-squares formulation for viscoelastic fluids, J. Non-Newtonian Fluid Mech. 140 (1–3) (2006) 132–144.
[22] X. Li, X. Han, X. Wang, Numerical modeling of viscoelastic flows using equal low-order finite elements, Comput. Methods Appl. Mech. Eng. 199 (2010) 570–581.
[23] P. Nithiarasu, A fully explicit characteristic based split (CBS) scheme for viscoelastic flow calculations, Int. J. Numer. Meth. Engng. 60 (2004) 949–978.
[24] T.F. Chen, C.L. Cox, H.C. Lee, K.L. Tung, Least-squares finite element methods for generalized Newtonian and viscoelastic flows, Appl. Numer. Maths. 60 (2010) 1024–1040.
[25] H.C. Lee, A nonlinear weighted least-squares finite element method for the Oldroyd-B viscoelastic flow, Appl. Math. Comp. 219 (2012) 421–434.
[26] J. Kwack, A. Masud, A three-field formulation for incompressible viscoelastic fluids, Int. J. of Eng. Sci. 48 (11) (2010) 1413–1432.
[27] E. Castillo, R. Codina, Variational multi-scale stabilized formulations for the stationary three-field incompressible viscoelastic flow problem, Comput. Methods Appl. Mech. Eng. 279 (2014) 579–605.
[28] R. Becker, M. Braack, A finite element pressure gradient stabilization for the Stokes equations based on local projections, Calcolo 38 (2001) 173–199.
[29] R. Becker, M. Braack, A two-level stabilization scheme for the Navier-Stokes equations, in: M. Feistauer, V. Dolejší, P. Knobloch, K. Najzar (Eds.), Numerical Mathematics and Advanced Applications, Springer-Verlag (Berlin), 2004, pp. 123–130.
[30] M. Braack, E. Burman, Local Projection Stabilization for the Oseen problem and its interpretation as a Variational Multiscale method, SIAM J. Numer. Anal. 43 (2006) 2544–2566.
[31] G. Matthies, P. Skrzypacz, L. Tobiska, A unified convergence analysis for local projection stabilisations applied to the Oseen problem, Math. Model. Numer. Anal. 41 (2007) 713–742.
[32] S. Ganesan, G. Matthies, L. Tobiska, Local projection stabilization of equal order interpolation applied to the Stokes problem, Math. of Comput. 77 (264) (2008) 2039–2060.
[33] S. Ganesan, L. Tobiska, Stabilization by local projection for convection-diffusion and incompressible flow problems, J. Sci. Comput. 43 (3) (2010) 326–342.
[34] M. Braack, G. Lube, Finite elements with Local Projection Stabilization for incompressible flow problems, J. Comp. Maths. 27 (2–3) (2009) 116–147.
[35] M.A. Alves, F.T. Pinho, P.J. Oliveira, The flow of viscoelastic fluids past a cylinder: finite-volume high-resolution methods, J. Non-Newtonian Fluid Mech. 97 (2001) 207–232.
[36] M.A. Hulsen, R. Fattal, R. Kupferman, Flow of viscoelastic fluids past a cylinder at high Weissenberg number: Stabilized simulations using matrix logarithms, J. Non-Newtonian Fluid Mech. 127 (2005) 27–39.
[37] E. Castillo, R. Codina, First, second and third order fractional step methods for the three-field viscoelastic flow problem, J. Comput. Phys. 296 (2015) 113–137.
[38] T.W. Pan, J. Hao, R. Glowinski, On the simulation of a time-dependent cavity flow of an Oldroyd-B fluid, Int. J. Numer. Meth. Fluids 60 (2009) 791–808.
[39] R.G. Sousa, R.J. Poole, A.M. Afonso, F.T. Pinho, P.J. Oliveira, A. Morozov, M.A. Alves, Lid-driven cavity flow of viscoelastic liquids, J. Non-Newtonian Fluid Mech. 234 (2016) 129–138.
[40] F.P. Martins, C.M. Oishi, A.M. Afonso, M.A. Alves, A numerical study of the kernel-conformation transformation for transient viscoelastic fluid flows, J. Comput. Phys. 302 (2015) 653–673.
[41] W. Zhou, J. Ouyang, X. Wang, J. Su, B. Yang, Numerical simulation of viscoelastic fluid flows using a robust FVM framework on triangular grid, J. Non-Newtonian Fluid Mech. 236 (2016) 18–34.
[42] K. Yapici, B. Karasozen, Y. Uludag, Finite volume simulation of viscoelastic laminar flow in a lid-driven cavity, J. Non-Newtonian Fluid Mech. 164 (2009) 51–65.
[43] M. Fortin, R. Pierre, On the convergence of the mixed method of Crochet and Marchal for viscoelastic flows, Comput. Methods Appl. Mech. Eng. 73 (3) (1989) 341–350.
[44] F.P.T. Baaijens, Mixed finite element methods for viscoelastic flow analysis: a review, J. Non-Newtonian Fluid Mech. 79 (1998) 361–385.
[45] F.P.T. Baaijens, M.A. Hulsen, P.D. Anderson, The Use of Mixed Finite Element Methods for Viscoelastic Fluid Flow Analysis, John Wiley and Sons, Ltd, 2004.
[46] A. Bonito, E. Burman, A continuous interior penalty method for viscoelastic flows, SIAM J. Sci. Comput. 30 (3) (2008) 1156–1177.
[47] A. Bonito, P. Clement, M. Picasso, Mathematical and numerical analysis of a simplified time-dependent and viscoelastic flow, Numer. Math. 107 (2007) 213–255.
[48] J. Bonvin, M. Picasso, R. Stenberg, GLS and EVSS methods for a three-field Stokes problem arising from viscoelastic flows, Comput. Methods Appl. Mech. Eng. 190 (2001) 3893–3914.
[49] E. Castillo, R. Codina, Numerical analysis of a stabilized finite element approximation for the three-field linearized viscoelastic fluid problem using arbitrary interpolations, ESAIM Mathematical Modelling and Numerical Analysis (2017). doi:10.1051/m2an/2016068.
[50] V.J. Ervin, W.W. Miles, Approximation of time-dependent viscoelastic fluid flow: SUPG approximation, SIAM J. Numer. Anal. 41 (2) (2003) 457–486.
[51] S. Ganesan, L. Tobiska, Finite Elements : Theory and Algorithms, Cambridge-I-ISc Series, Cambridge University Press, 2017.
[52] P.R. Amestoy, I.S. Duff, J.Y. L'Excellent, J. Koster, A fully asynchronous multifrontal solver using distributed dynamic scheduling, SIAM J. Matrix Anal. Appl. 23 (1) (2001) 15–41.

[53] P.R. Amestoy, A. Guermouche, J.Y. L'Excellent, S. Pralet, Hybrid scheduling for the parallel solution of linear systems, Parallel Comput. 32 (2) (2006) 136–156.
[54] U. Wilbrandt, C. Bartsch, N. Ahmed, N. Alia, F. Anker, L. Blank, A. Caiazzo, S. Ganesan, S. Giere, G. Matthies, R. Meesala, A. Shamim, J. Venkatesan, V. John, ParMooN – A modernized program package based on mapped finite elements, Comput. and Maths. with Appl. 74 (1) (2017) 74–88.
[55] S. Ganesan, V. John, G. Matthies, R. Meesala, S. Abdus, U. Wilbrandt, An object oriented parallel finite element scheme for computing PDEs: Design and implementation, IEEE 23rd International Conference on High Performance Computing Workshops, (HiPCW) (2016) 106–115–, doi:10.1109/HiPCW.2016.023.
[56] N. Ahmed, G. Matthies, L. Tobiska, H. Xie, Discontinuous Galerkin time stepping with local projection stabilization for transient convection-diffusion-reaction problems, Comput. Methods Appl. Mech. Engrg. 200 (21–22) (2011) 1747–1756.
[57] J.R. Shewchuk, Triangle: Engineering a 2D Quality Mesh Generator and Delaunay Triangulator, in: M.C. Lin, D. Manocha (Eds.), Applied Computational Geometry: Towards Geometric Engineering, Lecture Notes in Computer Science, volume 1148, Springer-Verlag, 1996, pp. 203–222. From the First ACM Workshop on Applied Computational Geometry
[58] J.R. Shewchuk, Delaunay refinement algorithms for triangular mesh generation, Computat. Geom. 22 (1–3) (2002) 21–74.
[59] V. John, G. Matthies, Higher-order finite element discretizations in a benchmark problem for incompressible flows, Int. J. Numer. Meth. Fluids 37 (2001) 885–903.
[60] P. Pakdel, S.H. Spiegelberg, G.H. McKinley, Cavity flows of elastic liquids: Two-dimensional flows, Phys. Fluids 9 (1997) 3123–3140.